GROUND BASED INTERFEROMETRIC RADAR INITIAL LOOK AT LONGVIEW, BLUE SPRINGS, TUTTLE CREEK, AND MILFORD DAMS

A Thesis presented to the Faculty of the Graduate School

University of Missouri-Columbia

In Partial Fulfillment

of the Requirements for the Degree

Master of Science

---

by

HUAZENG DENG

Dr. Justin J. Legarsky, Thesis Supervisor

JULY 2012

The undersigned, appointed by the Dean of the Graduate School, have examined the thesis entitled

GROUND BASED INTERFEROMETRIC RADAR INITIAL LOOK AT LONGVIEW, BLUE SPRINGS, TUTTLE CREEK, AND MILFORD DAMS

Presented by Huazeng Deng

A candidate for the degree of Master of Science

And hereby certify that in their opinion it is worthy of acceptance.

_____

Dr. Justin Legarsky

_____

Dr. Zhihai He

_____

Dr. Brent Rosenblad

ACKNOWLEDGEMENTS

During the course of this thesis work, I received enormous support from many people to whom I would like to express my gratitude.

First, I would like to thank my academic advisor, Dr. Justin Legarsky, for introducing me to this fascinating ground-based radar project and guiding me through my research career at MU, which finally leads to the fulfillment of this thesis. During the past two years' research with him, he has provided me with an amount of insightful advices, patience to solve my doubts, as well as the encouragements when I came across challenges in my research. The valuable research skills I gained from him will do a great help in my academic career. Also, I really appreciate the time and patience he spent on reviewing and revising my thesis. Without his generous help, I could hardly accomplish a thesis like this.

I would also like to thank my other thesis committee members, Dr. Brent Rosenblad and Dr. Zhihai He, for sparing time from their busy schedules to serve in my thesis committee. They made great efforts to revise my thesis by providing me with valuable suggestions and relevant comments on my writing as well as formatting of the thesis.

In addition, I'm grateful to those gorgeous people I worked with in this GBIR project. Dr. Paco Francisco spared no effect in teaching me patiently how to use Gamma software and leading me to study on the radar interferometry. Bjorn Held spent lots of time answering my questions and solving my doubts during the course of this

project. And Wyatt Jenkins, my nice friend and coworker in the research group, made great efforts in running most of field experiments with me. We went through difficulties and overcame the challenges together upon a number of experiments. These guys gave me so much support through this project and I wouldn’t have headed so far without their help.

Finally, I would like to express my sincere thanks to my beloved families and friends. Their constant support and encouragements have given me great confidence in overcoming difficulties in my study since I was a little kid and will continue to stimulate me to move on in my future academic career.

TABLE OF CONTENTS

ACKNOWLEDGEMENTS ii

TABLE OF CONTENTS iv

LIST OF TABLES viii

LIST OF FIGURES ix

ABSTRACT xvi

Chapter 1. Introduction 1

1.1 Satellite-Based-RADAR Deformation Measurement 1

1.2 MU Ground-Based-RADAR for Deformation Measurement 2

1.3 Thesis Overview and Organization 3

Chapter 2. RADAR Methodologies 4

2.1 RADAR FUNDAMENTALS OVERVIEW 4

2.2 RAR IMAGING 7

2.3 RADAR INTERFEROMETRY 10

2.4 RADAR POLARIMETRY 12

2.5 RADAR POLARIMETRIC INTERFEROMETRY 14

2.6 GBIR 14

Chapter 3. GBIR Horn Antenna and TCR 21

3.1 Introduction 21

3.2 Design of the horn antenna adapter 22

3.2.1 Hardware information description 22

3.2.2 Overall description of the horn adapter 23

3.2.3 Dimension specifications of the adapter 25

3.2.4 Horn Adapter Photographs 26

3.3 Trihedral Corner Reflectors 28

Chapter 4. Field Sites Description 32

4.0 Introduction 32

4.1 Longview Dam 33

4.1.1 Site information 33

4.1.2 Site overview 34

4.1.3 Site zoom 35

4.1.4 Site pins distribution 35

4.1.5 Site pin photos 36

4.2 Blue Springs Dam 37

4.2.1 Site information 37

4.2.2 Site overview 37

4.2.3 Site zoom 38

4.2.4 Site pins distribution 38

4.2.5 Site pin photos 39

4.3 Tuttle Creek Dam 40

4.3.1 Site information 40

4.3.2 Site overview 40

4.3.3 Site zoom 41

4.3.4 Site pins distribution 41

4.3.5 Site pin photos 42

4.4 Milford Dam 43

4.4.1 Site information 43

4.4.2 Site overview 43

4.4.3 Site zoom 44

4.4.4 Site pins distribution 44

4.4.5 Site pin photos 45

Chapter 5. GBIR Imagery from Field Sites 46

5.1 Introduction 46

5.2 Image processing results of Longview Dam 47

5.2.1 Pin 1 at Longview Dam 47

5.2.2 Pin 3 at Longview Dam 50

5.2.3 Pin 4 at Longview Dam 52

5.2.4 Pin 5 at Longview Dam 53

5.3 Image processing results of Blue Springs Dam 56

5.3.1 Pin 2 at Blue Springs Dam 56

5.4 Image processing results of Tuttle Creek Dam 60

5.4.1 Pin 1 at Tuttle Creek Dam 60

5.4.2 Pin 5 at Tuttle Creek Dam 64

5.5 Image processing results of Milford Dam 68

5.5.1 Pin 1 at Milford Dam 68

5.5.2 Pin 3 at Milford Dam 73

5.5.3 Pin 5 at Milford Dam 77

5.6 Summary 86

Chapter 6. Conclusion and Future Work 88

References 90

Appendix A GAMMA Software for GBIR Measurement and Data Processing 92

Appendix B The List of Values for Parameters Associated with the Decimation Factor for Each Test Site 98

LIST OF TABLES

Table Page

2-1. GBIR Specification Summary. 16

2-2. GBIR 2m Antenna Instrument Specification Summary. 16

2-3. GBIR Horn Antenna Instrument Specification Summary. 16

3-1. RCS values for various TCRs. 29

4-1. Field sites location and name is given. 33

LIST OF FIGURES

Figure Page

2-1. Block diagram illustrates simplified monostatic RADAR [Mahafza, 2000]. 5

2-2. A two target RAR imaging scenario is shown. The block diagram and time return illustrate the behavior of waveform with an effective pulse length, τ, and a range resolution, ΔR [Richards, 2005]. 9

2-3. Diagram illustrates RADAR interferometry concept [Elachi and van Zyl, 2006].....11

2-4. Diagram illustrates polarimetric RADAR measurement concept [Elachi and van Zyl, 2006].....13

2-5. Photos illustrate various setup configurations of the GBIR. a) Ku-band 2-m antenna setup is shown. b) C-/Ku-band horn antenna setup is shown. The three antennas positions may be denoted starting from the top as above, upper, and lower. 17

2-6. Photos illustrate various connections and setup of the GBIR polarimetric mode. a) C-band RF unit connections are identified. b) C-band 2-m dual-polarized antennas are shown mounted on the GBIR tower.....18

3-1. Antenna tower photos are shown. a) Antenna holding brackets are attached to the antenna tower by the red-colored hardware. b) The

antenna brackets are shown in close up. 22

3-2. Outline drawing illustrates the dimensions of the horn antenna. 23

3-3. CAD outline drawing of the antenna adapter is shown. 25

3-4. CAD drawing of the antenna adapter's top view is shown. 26

3-5. CAD drawing of the antenna adapter's front view is shown. 26

3-6. CAD drawing of the antenna adapter's side view is shown. 26

3-7. Photographs of the finished antenna adapters assembly are shown. a) Antenna adapters are shown on the tower (front view). b) Antenna adapters are shown on the tower (side view). 27

3-8. Photograph of the horn antennas mounted to the GBIR system is shown. 28

3-9. TCR using thick aluminum plates is shown (front view). 30

3-10. TCR using thick aluminum plates (one side shown). Hypotenuse is ~ 12". 30

3-11. Diagram shows the steps for making a small TCR from a single sheet. 31

3-12. A low-cost TCR is shown. 31

4-1.1. Google Earth view of Longview Dam is shown. 34

4-1.2. Google Earth zoomed-in view of Longview Dam is shown. 35

4-1.3. Site pins distribution at Longview Dam is illustrated. 35

4-1.4. Photographs from each pin location at Longview Dam are

presented. a) Pin 1, b) Pin 2, c) Pin 3, d) Pin 4, and e) Pin 5. 36

4-2.1. Google Earth view of Blue Springs Dam is shown. 37

4-2.2. Google Earth zoomed-in view of Blue Springs Dam is shown. 38

4-2.3. Site pins distribution at Blue Springs Dam is shown. 38

4-2.4. Photographs from each pin location at Blue Springs Dam are presented. a) Pin 1, b) Pin 2, c) Pin 3, d) Pin 4, and e) Pin 5. 39

4-3.1. Google Earth view of Tuttle Creek Dam is shown. 40

4-3.2. Google Earth zoomed-in view of Tuttle Creek Dam is shown. 41

4-3.3. Site pins distribution at Tuttle Creek Dam is shown. 41

4-3.4. Photographs from each pin location at Tuttle Creek Dam are presented. a) Pin 1, b) Pin 2, c) Pin 3, d) Pin 4, and e) Pin 5. 42

4-4.1. Google Earth view of Milford Dam is shown. 43

4-4.2. Google Earth zoomed-in view of Milford Dam is shown. 44

4-4.3. Site pins distribution at Milford Dam is illustrated. 44

4-4.4. Photographs from each pin location at Milford Dam are presented. a) Pin 1, b) Pin 3, and c) Pin 5. 45

5-2.1. Ku-band MLI image in radar coordinates for Pin 1 at Longview Dam on 02/17/2012 is shown. The 2-m antenna is used. 49

5-2.2. Ku-band MLI image in rectangular coordinates for Pin 1 at Longview Dam on 02/17/2012 is shown. The 2-m antenna is used. 49

5-2.3. Ku-band single pass interferogram for Pin 1 at Longview Dam on

02/17/2012 is shown. The 2-m antenna is used. 50

5-2.4. Ku-band MLI image in radar coordinates for Pin 3 at Longview Dam on 08/02/2011 is shown. The horn antenna is used.....51

5-2.5. Ku-band MLI image in rectangular coordinates for Pin 3 at Longview Dam on 08/02/2011 is shown. The horn antenna is used.....52

5-2.6. Ku-band MLI image in radar coordinates for Pin 4 at Longview Dam on 08/01/2011. The horn antenna is used.....53

5-2.7. Ku-band MLI image in rectangular coordinates for Pin 4 at Longview Dam on 08/01/2011. The horn antenna is used.....53

5-2.8. Ku-band MLI image in radar coordinates for Pin 5 at Longview Dam on 08/02/2011 is shown. The 2-m antenna is used.....54

5-2.9. Ku-band MLI image in rectangular coordinates for Pin 5 at Longview Dam on 08/02/2011 is shown. The 2-m antenna is used. 55

5-2.10. Ku-band single pass interferogram for Pin 5 at Longview Dam on 08/02/2011 is shown. The 2-m antenna is used. 56

5-3(a). C-band (HH) MLI image in rectangular coordinates for Pin 2 at Blue Springs Dam on 02/18/2012 is shown. The 2-m antenna is used....57

5-3(b). C-band (VH) MLI image in rectangular coordinates for Pin 2 at Blue Springs Dam on 02/18/2012 is shown. The 2-m antenna is used....58

5-3(c). C-band (HV) MLI image in rectangular coordinates for Pin 2 at Blue Springs Dam on 02/18/2012 is shown. The 2-m antenna is used....59

5-3(d). C-band (VV) MLI image in rectangular coordinates for Pin 2 at Blue Springs Dam on 02/18/2012 is shown. The 2-m antenna is used.....60

5-4.1. Ku-band MLI image in radar coordinates for Pin 1 at Tuttle Creek Dam on 09/16/2011 is shown. The 2-m antenna is used.....61

5-4.2. Ku-band MLI image in rectangular coordinates for Pin 1 at Tuttle Creek Dam on 09/16/2011 is shown. The 2-m antenna is used. 62

5-4.3. Ku-band single pass interferogram for Pin 1 at Tuttle Creek Dam on 09/16/2011 is shown. The 2-m antenna is used. 63

5-4.4. Ku-band repeat pass interferogram for Pin 1 at Tuttle Creek Dam on 09/16/2011-02/17/2012 is shown. The 2-m antenna is used. 64

5-4.5. Ku-band MLI image in radar coordinates for Pin 5 at Tuttle Creek Dam on 09/16/2011 is shown. The 2-m antenna is used.....65

5-4.6. Ku-band MLI image in rectangular coordinates for Pin 5 at Tuttle Creek Dam on 09/16/2011 is shown. The 2-m antenna is used. 66

5-4.7. Ku-band single pass interferogram for Pin 5 at Tuttle Creek Dam on 09/16/2011 is shown. The 2-m antenna is used. 67

5-4.8. Ku-band one day repeat pass interferogram for Pin 5 at Tuttle Creek Dam on 09/16/2011 is shown. The 2-m antenna is used. 68

5-5.1. Ku-band MLI image in rectangular coordinates for Pin 1 at Milford Dam on 09/16/2011 is shown. The 2-m antenna is used. 69

5-5.2. Ku-band MLI image in rectangular coordinates for Pin 1 at

Milford Dam on 09/16/2011 is shown. The 2-m antenna is used. 70

5-5.3. Ku-band single pass interferogram for Pin 1 at Milford Dam on 09/16/2011 is shown. The 2-m antenna is used. 71

5-5.4. Ku-band repeat pass interferogram for Pin 1 at Milford Dam 09/16/2011-02/17/2012 is shown. The 2-m antenna is used. 72

5-5.5. C-band (HH) repeat pass interferogram for Pin 1 at Milford Dam 11/18/2011-02/17/2012 is shown. The 2-m antenna is used. 73

5-5.6. Ku-band MLI image in radar coordinates for Pin 3 at Milford Dam is shown. The 2-m antenna is used.....74

5-5.7. Ku-band MLI image in rectangular coordinates for Pin 3 at Milford Dam on 09/17/2011 is shown. The 2-m antenna is used. 75

5-5.8. Ku-band single pass interferogram for Pin 3 at Milford Dam on 09/17/2011 is shown. The 2-m antenna is used. 76

5-5.9. Ku-band repeat pass interferogram for Pin 3 at Milford Dam 09/17/2011-02/17/2012 is shown. The 2-m antenna is used. 77

5-5.10. Ku-band MLI image in radar coordinates for Pin 5 at Milford Dam on 09/17/2011 is shown. The 2-m antenna is used.....79

5-5.11. Ku-band MLI image in rectangular coordinates for Pin 5 at Milford Dam on 09/17/2011 is shown. The 2-m antenna is used. 79

5-5.12. C-band fully polarimetric MLI images in rectangular coordinates for Pin 5 at Milford Dam on 10/07/2011(From left top to right bottom

are HH, VH, HV, VV) are shown. The 2-m antenna is used.....80

5-5.13. Ku-band single pass interferogram for Pin 5 at Milford Dam on 09/17/2011 is shown. The 2-m antenna is used. 81

5-5.14. Ku-band repeat pass interferogram for Pin 5 at Milford Dam 09/17/2011-02/17/2012 is shown. The 2-m antenna is used.....82

5-5.15. C-band(HH) repeat pass interferogram for Pin 5 at Milford Dam 10/07/2011-02/17/2012 is shown. The 2-m antenna is used.....83

5-5.16. C-band(VH) repeat pass interferogram for Pin 5 at Milford Dam 10/07/2011-02/17/2012 is shown. The 2-m antenna is used.....84

5-5.17. C-band(HV) repeat pass interferogram for Pin 5 at Milford Dam 10/07/2011-02/17/2012 is shown. The 2-m antenna is used..... 85

5-5.18. C-band (VV) repeat pass interferogram for Pin 5 at Milford Dam 10/07/2011-02/17/2012 is shown. The 2-m antenna is used.....86

GROUND BASED INTERFEROMETRIC RADAR INITIAL LOOK AT LONGVIEW, BLUE SPRINGS, TUTTLE CREEK, AND MILFORD DAMS

Huazeng Deng

Dr. Justin J. Legarsky, Thesis Supervisor

ABSTRACT

Measuring millimeter and smaller deformation has been demonstrated in the literature using RADAR. To address in part the limitations in current commercial satellite-based SAR datasets, a University of Missouri (MU) team worked with GAMMA Remote Sensing to develop a specialized (dual-frequency, polarimetric, and interferometric) ground-based real-aperture RADAR (GBIR) instrument. The GBIR device is portable with its tripod system and control electronics. It can be deployed to obtain data with high spatial resolution (i.e. on the order of 1 meter) and high temporal resolution (i.e. on the order 1 minute). The high temporal resolution is well suited for measurements of rapid deformation. From the same geodetic position, the GBIR may collect dual frequency data set using C-band and Ku-band. The overall goal of this project is to measure the deformation from various scenarios by applying the GBIR system. Initial efforts have been focusing on testing the system performance on different types of targets.

This thesis details a number of my efforts on experimental and processing activities at the start of the MU GBIR imaging project. For improved close range capability, a wideband dual polarized antenna option was produced and tested. For GBIR calibration, several trihedral corner reflectors were designed and fabricated. In addition to experimental activities and site selection, I participated in advanced data processing activities. I processed GBIR data in several ways including single-look-complex (SLC) image generation, imagery registration, and interferometric processing. A number of initial-processed GBIR image products are presented from four dams: Longview, Blue Springs, Tuttle Creek, and Milford. Excellent imaging performance of the MU GBIR has been observed for various target types such as riprap, concrete, soil, rock, metal, and vegetation. Strong coherence of the test scene has been observed in the initial interferograms.

Chapter 1. Introduction

1.1 Satellite-Based-RADAR Deformation Measurement

Commercial satellite-based synthetic-aperture RADAR interferometry (INSAR) techniques may be used for measuring deformation from various scenarios such as landslides, glacier movement, underground liquid extraction, mining, and tectonic motion. Sophisticated synthetic-aperture RADAR (SAR) techniques utilizing the phase and amplitude of return signals may produce longer antenna effective lengths (e.g. narrower beam) from a smaller physical antenna length (e.g. broader beam). For interferometric SAR (INSAR), an interferogram may be formed from the phase difference between two SAR images of an area. From the interferogram, the line-of-sight (LOS) range is measured accurately. These accurate range measurements allow generation of digital elevation models (DEMs) and surface deformations. Differential interferometric synthetic-aperture RADAR (DINSAR) may further improve the phase sensitivity to surface displacement by reducing other contributions such as from topography. With satellite DINSAR, centimeter-scale surface deformations may be measured [Elachi and van Zyl, 2006]. For current commercially

available satellite SAR datasets, there exist a number of potential limitations such as spatial resolution, temporal resolution, operating frequency, and polarization.

1.2 MU Ground-Based-RADAR for Deformation Measurement

To address in part the limitations in current commercial satellite-based SAR datasets, a University of Missouri (MU) team worked with GAMMA Remote Sensing to develop a specialized (dual-frequency, polarimetric, and interferometric) ground-based real-aperture RADAR (GBIR) instrument. The GBIR device is portable with its tripod system and control electronics. It can be deployed to obtain data with high spatial resolution (i.e. on the order of 1 meter) and high temporal resolution (i.e. on the order of 1 minute). The high temporal resolution is well suited for measurements of rapid deformation. From the same geodetic position, the GBIR may collect dual frequency data sets using C-band and Ku-band. The scattering vector may be investigated using the GBIR fully polarimetric capability at C-band operation. MU GBIR may collect imagery for interferometric processing of both single-pass and repeat-pass configurations.

The MU GBIR system has been deployed in a number of field experiments. A number of United States Army Corps of Engineers (USACE) dams in Missouri and Kansas have been imaged with the GBIR. Imagery has been collected of 2 landfills in Colorado and Missouri. Millimeter scale sensitivity has been demonstrated using the MU GBIR.

1.3 Thesis Overview and Organization

This thesis details a number of my efforts on experimental and processing activities of the MU GBIR imaging project. The GBIR development was completed in two primary phases: a) Ku-band VV single polarization GBIR, and b) C-band fully polarimetric GBIR. During the MU GBIR development, experiment options and site selection was investigated. For GBIR calibration, several trihedral corner reflectors were designed and fabricated. For improved close range capability (e.g. range less than about 50 meters), a wideband dual polarized antenna option was produced. In addition to experimental activities, I participated in advanced data processing activities. I processed GBIR data in several ways including single-look-complex (SLC) image generation, imagery registration, interferometric processing, and differential interferometric processing. This thesis presents a number of results and images for each of the experimental sites.

Thesis organization includes an introduction in Chapter 1, an overview of Ground-Based Interferometric RADAR in Chapter 2, a description of the GBIR Horn Antenna Option and Trihedral Corner Reflector Development in Chapter 3, an account of the project field sites in Chapter 4, a presentation of a number of GBIR images and results in Chapter 5, a concluding discussion and future work direction in Chapter 6, and finally a listings of the thesis references in Chapter 7.

Chapter 2. RADAR Methodologies

An extensive body of open literature exists for RADAR and RADAR methodologies. This chapter provides a summary overview of the pertinent concepts and methods utilized in this study.

2.1 RADAR FUNDAMENTALS OVERVIEW

A RADAR sensor performs radio detection and ranging. Transmission and reception of electromagnetic (EM) waves may be facilitated by the use of antennas. The radiated EM wave may interact with matter (i.e. targets) resulting in EM scatter in the direction of the RADAR receive antenna. The received signal may be amplified and further processed upon reception to determine various ranging and detection information. The return signal's arrival time in conjunction with the media parameters (i.e. permittivity and permeability) may be used to determine target range. Figure 2-1 illustrates a simple pulsed RADAR using monostatic mode (i.e. transmitter and receiver collocated) [Mahafza, 2000].

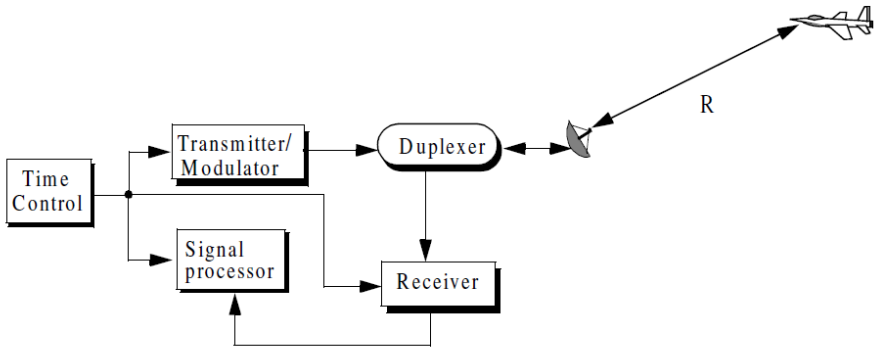

Figure 2-1. Block diagram illustrates simplified monostatic RADAR [Mahafza, 2000].

The EM wave transmitted by the RADAR antenna expands outwardly in the form of spherical waves. Far away from the RADAR, the spherical EM wave front appears approximately planar [Ulaby, 2007]. This far-field region may be defined for the ranges as follows [Richards, 2005]:

$$R_{\text{far field}} \geq \frac{2D^2}{\lambda} \tag{2.1}$$

where D refers to the antenna maximum dimension and λ is the wavelength. A transverse EM plane wave's vector amplitude may be written as [van Zyl and Kim, 2011]

$$\vec{A} = a_h e^{j\delta_h}\hat{h} + a_v e^{j\delta_v}\hat{v} \tag{2.2}$$

where $\hat{h}$ and $\hat{v}$ are the orthogonal (e.g. horizontal and vertical) unit vectors, a_h and a_v are real valued amplitudes, and δ_h and δ_v are the real valued relative phases. The shape traced out by the tip of the electric field over time at a fixed point in space refers to its polarization [van Zyl and Kim, 2011]. Thus for a monochromatic plane wave, the wave may be identified by measuring each orthogonal component's amplitude and

phase in such manner as to measure the polarization.

A radiation pattern describes the directional characteristic of an antenna. A common pattern for imaging radar uses a single main lobe surrounded by side lobes. The main lobe may be summarized by calculating its orthogonal half-power beam widths (one in azimuth β_{az} and the other in elevation β_{el}) and its maximum gain, *G*. The side lobes response may be summarized by the ratio of the maximum side lobe to the main lobe maximum. For dual fed orthogonally polarized antennas, the crosstalk from one feed to the other may summarize the antenna's polarization purity.

For received power consideration, a target's scattering behavior may be described by the RADAR cross section (RCS), σ. The RCS is an area quantity. If the power collected by an RCS area is reradiated isotropically (i.e. same in all directions), then the same scattered power density will be produced as by the actual target [Richards, 2005]. The monostatic radar range equation [Ulaby *et al*., 1982] for a target may be written as

$$P_r = \frac{P_t G^2 \lambda^2 \sigma}{(4\pi)^3 R^4} \tag{2.3}$$

To calculate the ensemble average power over space and time for many targets, the differential scattering coefficient (i.e. sigma nought) is defined as the average value of the scattering cross-section per unit area [Ulaby *et al.*, 1982], written as

$$\sigma^0 = \langle \frac{\sigma_i}{\Delta A_i} \rangle \tag{2.4}$$

where σ_i is the radar cross section of target *i*, ΔA_i is the area associated with σ_i, and <> is the ensemble average operation. Assuming an effective pulse-limited scenario and near constant parameters and range over the illuminated area, the radar cross section

[Richards, 2005] may be written approximately as

$$\sigma = \sigma^0 A_{ill} \tag{2.5}$$

where A_{ill} is the illuminated area. A_{ill} may be approximated for a flat surface with small azimuth angle [Richards, 2005] as

$$r_{az} = 2Rsin\left(\frac{\beta_{az}}{2}\right) \approx R\beta_{az} \text{ for small angles and flat surface} \tag{2.6}$$

$$r_g = \frac{r_R}{sin\theta_{inc}} \text{ for flat surface} \tag{2.7}$$

$$A_{ill} = r_g r_{az} = \frac{r_R}{sin\theta_{inc}} R\beta_{az} \tag{2.8}$$

where r_g is the ground range resolution, r_{az} is the azimuth resolution, r_R is the slant range resolution, θ_{inc} is the associated look angle of incidence, R is the associated range, and β_{az} is the azimuth half-power beam width in units of radians. Under the mentioned assumptions, the monostatic pulse-limited area scatterers form of the radar range equation [Skolnik, 1990] may be written as

$$P_r = \frac{P_t G^2 \lambda^2 \sigma^0 A_{ill}}{(4\pi)^3 R^4} = \frac{P_t G^2 \lambda^2 \sigma^0 r_R \beta_{az}}{(4\pi)^3 R^3 sin\theta_{inc}} \quad . \tag{2.9}$$

2.2 RAR IMAGING

Moving-antenna real-aperture RADAR (RAR) may image a scene. Two major advantages of microwave RADAR imaging over visible optical imaging are imaging capabilities through weather (e.g. clouds) and day/night imaging capability [Richards, 2005]. For an antenna rotating horizontally about a fixed point, an EM wave may be transmitted and received as a function of the horizontal scan angle. The

following overview considers a flat surface. If the surface is not flat, then corrections for the topography may be required. The ground and azimuth resolutions determine how close two targets may be distinguished from one another in the ground and azimuth directions, respectively. The azimuth resolution is a function of the distance and the azimuth beam width as shown in equation 2.6. The ground resolution is a function of the incidence angle and the range resolution. The range resolution is determined by the wave's velocity of propagation, *v*, (i.e. speed of light) and the waveform bandwidth, *B*, [Elachi and Zyl, 2006] given as

$$r_R = \frac{v}{2B} = \frac{v\tau_{eff}}{2} \tag{2.10}$$

$$\tau_{eff} = \frac{1}{B} \tag{2.11}$$

where τ_{eff} is the effective pulse duration after matched filtering [Richards, 2005]. Linear frequency modulation (FM) is widely used in RADAR imaging. Thus, the waveform bandwidth plays a critical role in range resolution through the effective pulse length. A simple example of two closely spaced targets being RAR imaged is illustrated in Figure 2-2 [Richards, 2005].

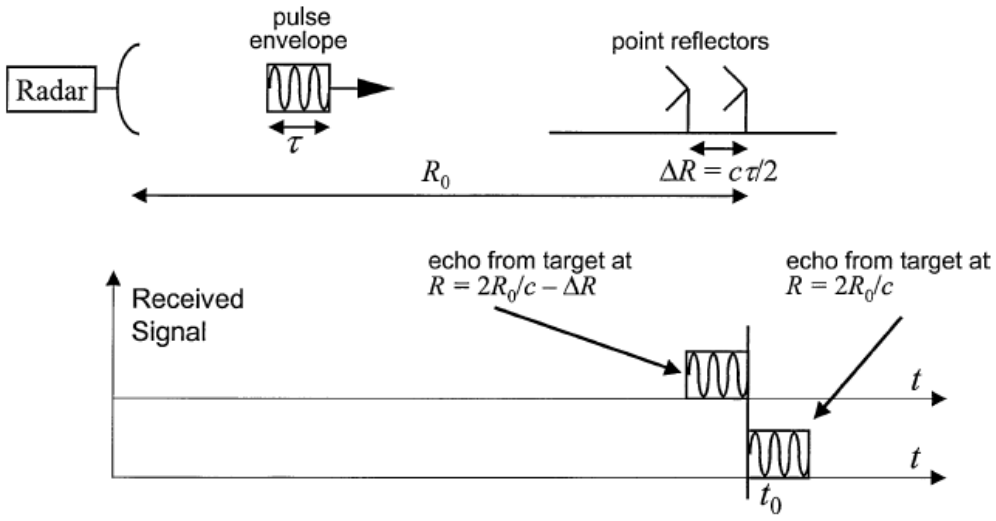

Figure 2-2. A two target RAR imaging scenario is shown. The block diagram and time return illustrate the behavior of waveform with an effective pulse length, τ, and a range resolution, ΔR [Richards, 2005].

From each effective pulse, a return signal in azimuth may be sampled. As the RAR imager scans in azimuth, *N* azimuth lines may be stored. For each azimuth line, typically *M* range bin samples are collected. The total angle scanned is θ_{scan} in degrees at the scan rate, $\Delta\theta$, in degrees per azimuth line. Thus, an *N* x *M* sized image may be formed in polar coordinates (e.g. N rows span the azimuth angles. M columns span the RADAR slant range). Polar to rectangular coordinate conversion may be applied to aid visualization in rectangular coordinate system. If the RAR collects more than 1 return signal per effective pulse, then decimation may be applied (i.e. anti-alias low pass filter followed by down sampling [Oppenheim and Schafer, 1989]). Decimation provides a signal-to-noise ratio improvement of approximately the decimation factor.

A decimation factor, *D*, based on minimum fraction of overlap, *K*, may be formed as follows:

$$D = \text{floor}\left\{\frac{N}{\theta_{scan}}\beta_{az}(1-K)\right\} = \text{floor}\left\{\frac{1}{\Delta\theta}\beta_{az}(1-K)\right\} \quad (2.12)$$

where floor is the mathematical operation of rounding down to the nearest integer. After decimation, there are *M* azimuth lines remaining given as

$$M = \text{floor}\left\{\frac{N}{D}\right\} = \text{floor}\left\{\frac{N\Delta\theta}{\beta_{az}(1-K)}\right\} \quad (2.13)$$

with an effective decimated scan rate given by

$$\Delta\theta_M = D\Delta\theta \quad (2.14)$$

For example, given K = 0.8 or 80% overlap for a 0.5° azimuth beam width would result in a decimated scan rate of about 0.1° (i.e. β_{az}(1-*K*)) since the floor function truncates the decimal point it may be slightly less than 0.1° as by equation 2.14.

2.3 RADAR INTERFEROMETRY

RADAR interferometry is one technique for the measurement of angles. The interferometric concept is based on the collection of two RADAR complex valued images either by two separated antennas or using repeated image collections. A brief summary overview [Hanssen, 2001] of RADAR interferometry follows. After aligning and resampling the two images, the multiplicative complex interferogram, *v*, may be formed as

$$y_1 = |y_1|e^{j\psi_1} \quad \text{image 1} \quad (2.15)$$

$$y_2 = |y_2|e^{j\psi_2} \quad \text{image 2} \quad (2.16)$$

$$v = y_1 y_2^* = |y_1||y_2|e^{j(\psi_1-\psi_2)} \quad (2.17)$$

where y_1, y_2 are complex valued, and ψ_1,ψ_2 are real valued. By referring to Figure 2-3

[Elachi and van Zyl, 2006], the measured interferometric phase may be approximately [Hanssen, 2001] a combination of topographic phase, displacement phase, and phase from everything else given as

$$\phi_p = \phi_{topography} + \phi_{displacement} + \phi_{everything\ else} = -\frac{4\pi}{\lambda}\Delta R \qquad (2.18)$$

where ΔR is the total apparent change in range between image 1 and image 2 to the surface. The height ambiguity is the height difference corresponding to a phase shift of 2π. The height ambiguity may be written as

$$h_{2\pi} = \left|\frac{\lambda R_{1,p} sin\theta_p^0}{2B_{\perp,p}^0}\right| \qquad (2.19)$$

where $B^0{}_{\perp,p}$ is the perpendicular baseline associated with the surface, $R_{1,p}$ is the range from image 1 to the surface, and $\theta^0{}_p$ is the look angle from image 1 to the point on the surface.

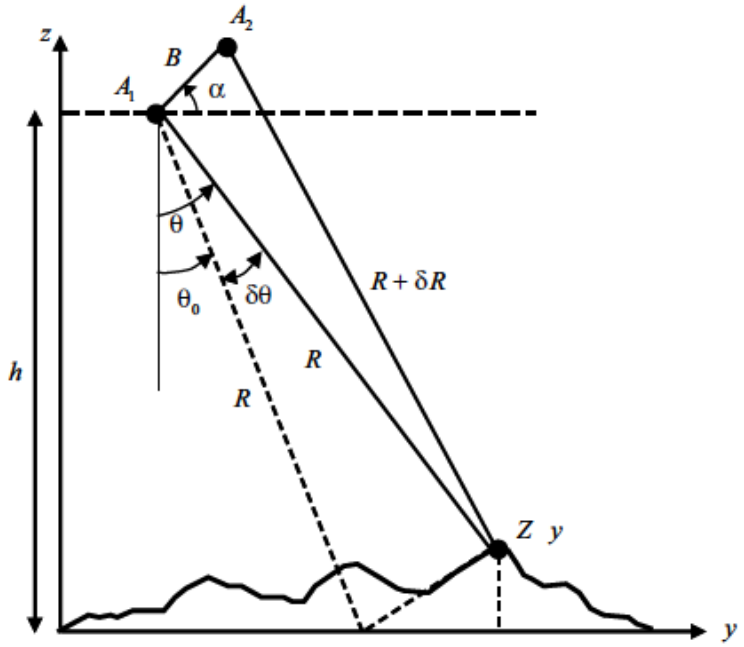

Figure 2-3. Diagram illustrates RADAR interferometry concept [Elachi and van Zyl, 2006].

Differential interferometry utilizes a data set consisting of a series of complex valued RADAR images acquired over time. If the images are acquired from exactly the same position, then there is no phase signal due to topography. Phase differences between successive images acquired from the same viewpoint are used to determine line-of-sight displacements from image acquisitions spaced temporally. Differential interferometry mapping of deformation can achieve accuracies in the millimeter level [Hanssen, 2001].

2.4 RADAR POLARIMETRY

Polarimetric RADARs measure the full scattering matrix. The received voltage may be written [van Zyl and Kim, 2011] as

$$V = c_a \mathbf{p}^{rec} \cdot [\mathbf{S}]\mathbf{p}^{tr} \tag{2.20}$$

where $\mathbf{p}^{rec}$, $\mathbf{p}^{tr}$ are the normalized receiving and transmitting polarization vectors and **S** is the scattering matrix given by

$$[\mathbf{S}] = \begin{pmatrix} S_{hh} & S_{hv} \\ S_{vh} & S_{vv} \end{pmatrix} \tag{2.21}$$

where the first subscript refers to receiving polarization and the second subscript refers to transmitting polarization. Inspection of equation 2.20 reveals that two components of the scattering matrix may be measured at a time by setting one transmit vector element to 1 and the other to 0 such as the following,

$$\begin{pmatrix} S_{hh} \\ S_{vh} \end{pmatrix} = \begin{pmatrix} S_{hh} & S_{hv} \\ S_{vh} & S_{vv} \end{pmatrix} \begin{pmatrix} 1 \\ 0 \end{pmatrix}^{tr} \tag{2.22}$$

$$\begin{pmatrix} S_{hv} \\ S_{vv} \end{pmatrix} = \begin{pmatrix} S_{hh} & S_{hv} \\ S_{vh} & S_{vv} \end{pmatrix} \begin{pmatrix} 0 \\ 1 \end{pmatrix}^{tr} \tag{2.23}$$

Polarimetric data may be acquired by pulse interleaving H and V transmitting pulses and receiving both H and V as shown in Figure 2-4 [Elachi and van Zyl, 2006].

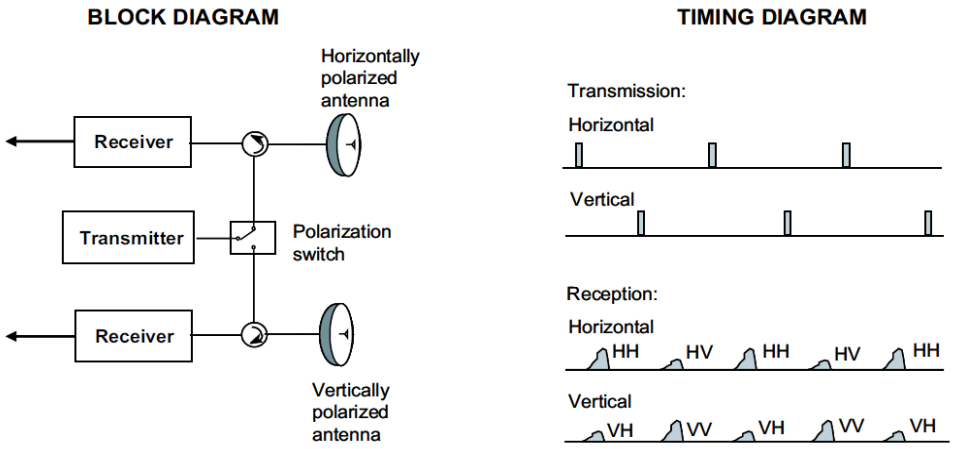

Figure 2-4. Diagram illustrates polarimetric RADAR measurement concept [Elachi and van Zyl, 2006].

A number of calibration techniques exist for polarimetric RADAR. Absolute calibration corrects a number amplitude and phase errors. Absolute calibration typically uses known targets, such as trihedral corner reflectors, spheres, and certain distributed targets [Papathanassiou and Mink, 1998]. A trihedral corner reflector's maximum RCS [Ulaby et. al, 1982] may be computed as

$$\sigma_{max} = \frac{4\pi}{\lambda^2}\frac{l^4}{12} \tag{2.24}$$

where l is the longest side of the reflector. Crosstalk calibration [Quegan, 1994] may be done before [e.g. Papathanassiou and Mink, 1998] or after absolute calibration [e.g. Fore *et al.*, 2009].

2.5 RADAR POLARIMETRIC INTERFEROMETRY

Polarimetric RADAR interferometry is described in detail in the literature [Cloude and Papathanassiou, 1998]. Here, a brief summary of the complex vector interferogram equation is given as

$$\mu_1\mu_2^* = \underline{\omega_1^{*T}}[\Omega_{12}]\underline{\omega_2} \tag{2.25}$$

where μ_1, μ_2 are the coefficients associated with the scattering matrices for image 1 and image 2 that project the scattering vectors onto the vectors ω_1, ω_2, and Ω_{12} is the scattering vectors covariance matrix. The interferogram's coherence may be optimized by

$$\mu_{1opt}\mu_{2opt}^* = \underline{\omega_{1opt}^{*T}}[\Omega_{12}]\underline{\omega_{2opt}} \tag{2.26}$$

where the optimization technique is detailed in the literature [Cloude and Papathanassiou, 1998].

2.6 GBIR

To address in part the limitations in current commercial satellite-based RADAR datasets, a MU team in conjunction with GAMMA Remote Sensing developed a specialized (dual-frequency, polarimetric, and interferometric) ground-based real-aperture RADAR (GBIR) instrument. A summary of the GBIR is presented here (see Table 2-1 for specifications summary) further details may be found in the user manual [GAMMA, 2011].

MU GBIR instrument uses real-aperture imaging. Three antennas may be mounted parallel to one another on a 1 meter high tower that may be precisely rotated. In the interferometric mode and single polarization mode, there is one antenna used to transmit and two receiving antennas. In fully polarimetric mode, one antenna transmits H polarization followed by V polarization repetitive sequence and one antenna receives both H and V returns. Figures 2-5 and 2-6 illustrate the various modes of the MU GBIR.

Table 2-1. GBIR Specification Summary.

Type	**C-Band Specification**	**Ku-band Specification**
Radar Type	FM-CW, chirps between 0.25 to 8 ms	FM-CW, chirps between 0.25 to 8 ms
Radar Modes	Fully Polarimetric (HH,HV,VH, and VV) Single Polarization (HH,HV,VH, or VV) Interferometric	Single Polarization 2m Antenna (VV) Single Polarization Horn (HH,HV,VH, or VV) Interferometric
Transmit Power	100 mW (+20 dBm)	100 mW (+20 dBm)
Chirp Bandwidth	200 MHz	200 MHz
Azimuth Scan Time	20 sec for 180 degree sweep	20 sec for 180 degree sweep
ADC	14-bit, dual channel, 6.25 MHz sample clock	14-bit, dual channel, 6.25 MHz sample clock

Table 2-2. GBIR 2m Antenna Instrument Specification Summary.

Type	**C-Band Specification**	**Ku-band Specification**
Frequency	5.3 to 5.5 GHz	17.1 to 17.3 GHz
2m Antenna Pattern	1.5 degree, 3 dB Azimuth Beamwidth 38 degree, 3 dB Elevation Beamwidth Peak sidelobes: -13 dB sidelobes (1-way)	0.5 degree, 3 dB Azimuth Beamwidth 38 degree, 3 dB Elevation Beamwidth Peak sidelobes: -15 dB sidelobes (1-way)
Antenna Polarization	Dual Polarized (H and V)	Single Polarization (V)
Radar operational Range	10 m – 10 km	10 m – 10 km
Azimuth Resolution	~26 m at 1 km, proportional to slant range	~9 m at 1 km, proportional to slant range
Range Resolution	0.75 m without weighting 1.0 m with Kaiser Weighting	0.75 m without weighting 1.0 m with Kaiser Weighting

Table 2-3. GBIR Horn Antenna Instrument Specification Summary.

Type	**C-Band Specification**	**Ku-band Specification**
Frequency	5.3 to 5.5 GHz	17.1 to 17.3 GHz
Horn Antenna Pattern	~35 degree, 3 dB Azimuth Beamwidth ~35 degree, 3 dB Elevation Beamwidth Peak sidelobes: -10 dB sidelobes (1-way)	~10 degree, 3 dB Azimuth Beamwidth ~20 degree, 3 dB Elevation Beamwidth Peak sidelobes: -10 dB sidelobes (1-way)
Antenna Polarization	Dual Polarized (H and V)	Dual Polarized (H and V)
Radar operational Range	< 500 m	< 500 m
Azimuth Resolution	~ 31 m at 50 m, proportional to slant range	~9 m at 50 m, proportional to slant range
Range Resolution	0.75 m without weighting 1.0 m with Kaiser Weighting	0.75 m without weighting 1.0 m with Kaiser Weighting

a)

b)

Figure 2-5. Photos illustrate various setup configurations of the GBIR. a) Ku-band 2-m antenna setup is shown. b) C-/Ku-band horn antenna setup is shown. The three antennas positions may be denoted starting from the top as above, upper, and lower.

For the fully polarimetric mode, Rx2 may attach to V Port (vertical) – upper, Rx1 may attach to H Port (horizontal) – lower, and TX H/V may attach to H/V Ports of the top antenna – above. Under this configuration, 4 single-look complex (slc) files may be generated [GAMMA, 2011] with the naming convention that follows:

1. Run once with gpri2_proc.py in -t TX_ANTENNA mode to V

    *Vu.slc VV (V receive, V transmit)
    *Vl.slc HV (H receive, V transmit)

2. Run second time with gpri2_proc.py in -t TX_ANTENNA mode to H

    *Hu.slc VH (V receive, H transmit)
    *Hl.slc HH (H receive, H transmit)

a) b)

Figure 2-6. Photos illustrate various connections and setup of the GBIR polarimetric mode. a) C-band RF unit connections are identified. b) C-band 2-m dual-polarized antennas are shown mounted on the GBIR tower.

A GBIR radar image may be acquired line by line by azimuthally rotating the antennas about the vertical axis. The antennas may be tilted vertically to illuminate the desired area. Also, the instrument has a digital chirp generator, a microwave assembly that contains the transmitter and 2 independent receivers, an analog to digital converter (ADC), and a laptop computer. The laptop computer controls the data acquisition and is used for later data analysis. The GBIR system can radiate microwaves at different frequencies, including C-band with a center frequency of 5.4 GHz and Ku-band with a center frequency of 17.2 GHz. The radar frequencies allow high sensitivity to motion in a number of varying scenarios. At C-band, the GBIR system has fully polarimetric capabilities. The longer wavelength at C-band enables stronger penetrating capabilities of the RADAR than at Ku-band for a number of scenarios. Two separate receiving antennas on the GBIR instrument allow differential interferometry on the scanned scene. A set of 2 m antennas or a set of dual-polarized horn antennas may be used. The fully polarimetric capabilities of MU GBIR system enable the application of polarimetric interferometry, scatterer decomposition, and other advanced polarimetric methods. The instrument is portable and may be battery operated. When employing an azimuth scan, a data collect takes 20 seconds for a 180 degree sweep. Appendix A provides GAMMA software processing commands with a number of examples.

Another distinct advantage of MU GBIR system lies in that this portable instrument may be removed and repositioned at the same point with high geodetic-grade precision. The standard setup of the GBIR system takes about 10 minutes and is reproducible.

Repeated field experiments can be performed at the same point with the help of the laser plummet on the instrument, GPS, and other markers.

Chapter 3. GBIR Horn Antenna and TCR

3.1 Introduction

This chapter focuses on the design effort for a number of hardware accessories for the GBIR system. The far-field beginning range of the 2-m antenna is about 150 m at C-band and about 500 m at Ku-band. To begin the far-field at a closer distance, compact horn antennas (i.e. physical aperture about 0.118 m by 0.118 m) were acquired. The far-field beginning range of this horn antenna is about 0.5 m at C-band and about 1.6 m at Ku-band. The horn antennas were acquired from Chengdu A-info Company for short-range scene mapping. As part of my research effort, an adapter was developed to allow attachment of these horn antennas to the GBIR antenna tower.

Advanced polarimetric processing and techniques often rely on precise amplitude and phase measurement. One way to improve the accuracy of the measurement is to apply absolute calibration, which corrects a number of amplitude and phase errors of the measured data. As discussed in Chapter 2, absolute calibration of GBIR data may be accomplished using known targets such as trihedral corner reflectors, spheres, and certain distributed targets. Here, we explored the fabrication of several low-cost known trihedral corner reflectors (TCR).

This chapter documents these research and development activities.

3.2 Design of the horn antenna adapter

3.2.1 Hardware information description

In order to assist the design procedure of the antenna adapter, a brief description of the antenna tower and horn antenna dimension specifications are provided. The antenna tower of GBIR is fixed on top of the motor on the tribrach using the tribrach level adjustment screws. At the back of the antenna tower, a RF unit is mounted on the mounting brackets of the tower. At the front of the antenna tower, three fan-beam antennas are mounted on the corresponding antenna holders (i.e. above, upper, and lower as described in chapter 2). The antenna holders can be adjusted to angles between -45° and +45°. The antenna tower and holders on it are shown in Figure 3-1.

a) b) 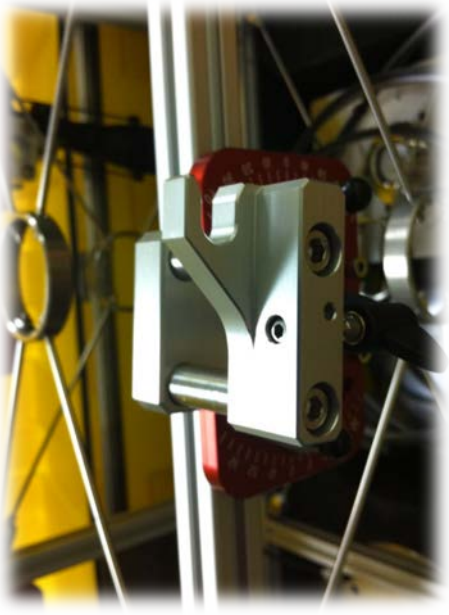

Figure 3-1. Antenna tower photos are shown. a) Antenna holding brackets are attached to the antenna tower by the red-colored hardware. b) The antenna brackets are shown in close up.

For targets in a comparatively shorter range (e.g. <500 m), we utilize small horn antennas for the GBIR. The horn antennas applied in our experiments operate over the frequency range 2 - 18GHz and are dual polarized. The horns were designed by A-INFO company in Chengdu, China. Its serial number is JXTXLB-SJ-20180. The dimension of this horn antenna is 118 mm x118 mm x187 mm. The outline sketch of the horn antenna is shown in Figure 3-2.

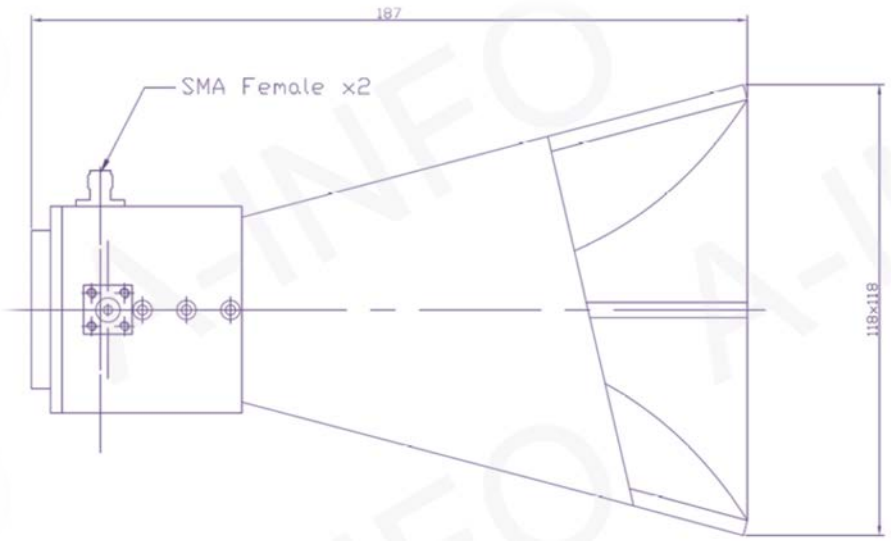

Figure 3-2. Outline drawing illustrates the dimensions of the horn antenna.

3.2.2 Overall description of the horn adapter

The design of the antenna adapter went through a number of iterations. The basic design strategy used a rectangular-shaped metal plate as the antenna bracket. At the center of the metal plate, precisely placed holes were drilled for the screws to mount the

horn antenna. The shape of the two ends of the plate is critical in the mechanical matching. Since we plan to take advantage of the existed antenna holders on the tower, we cut a slot at each end of the plate and put a rod going through each slot. In this way, we slid a rod into the hook of the holder. Wing nuts fix both ends of the adapter to the antenna tower. The distance was precisely measured between the rod center and the back face of the plate in order to keep the plate standing vertically when slid into the holders. Also, the back face of the plate must match well with the surface of the extended part of the holder.

To avoid the edge of the plate being blocked by the rods on the tower when it is rotated to the maximum angle (i.e. ±45°), we added two metal pieces to the back of the plate and moved the rods into these two metal pieces. In the back center of the plate, a circular slot was cut and several holes were drilled according to the hole patterns of the horn antenna.

Thus, the horn antenna can first be fixed onto the plate using screws and then the adapter can be slid into the antenna holders on the tower. Finally, the adapter can be tightened onto the extended parts of the holders by simply screwing the wing nuts on the holder. The material we chose for the plate is aluminum. The total weight of these three brackets plus the horn antennas is close to that of the RF unit (~ 4kg). Thus, the balance of the tower is retained well.

3.2.3 Dimension specifications of the adapter

The antenna adapters are designed based on the dimension specification of the tower and the shape of the holders. To make the back face of the adapter fit well with the holders, it is necessary to do the measurement precisely and design the bracket according to the dimension specifications. Fortunately, we acquired a digital file of the tower structure from Gamma Remote Sensing AG and obtained the precise dimensions of the tower with the help of ProE Software. Using the collected dimension information, we designed the horn antenna bracket finally in Auto CAD. The outline drawing of the antenna bracket is shown in Figure 3-3.

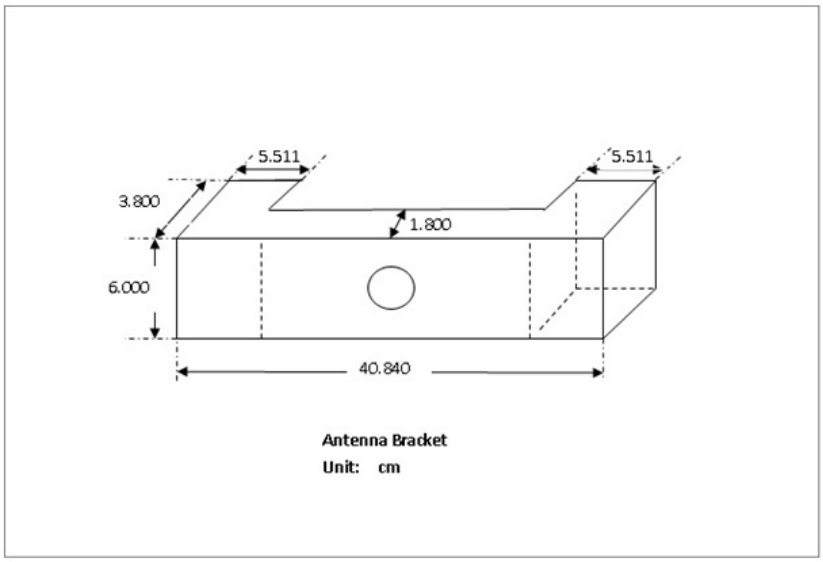

Figure 3-3. CAD outline drawing of the antenna adapter is shown.

Pictures at different views of the antenna bracket designed under Auto CAD environment are shown below:

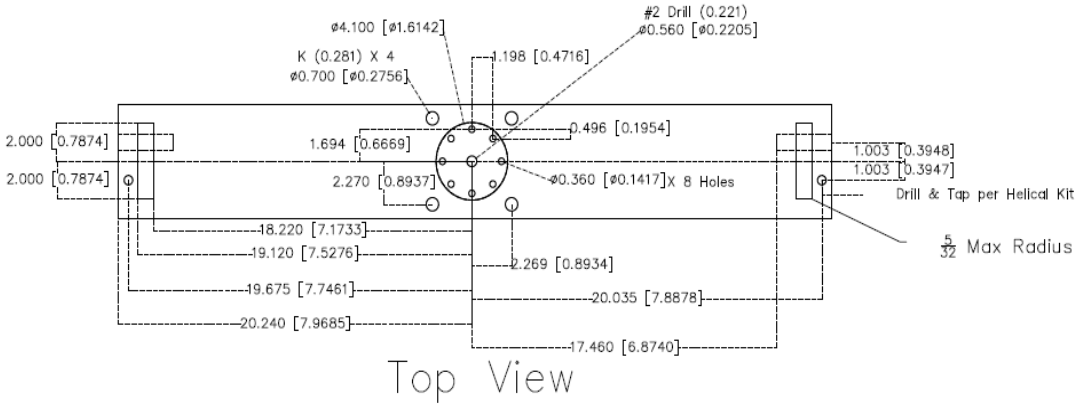

Figure 3-4. CAD drawing of the antenna adapter's top view is shown.

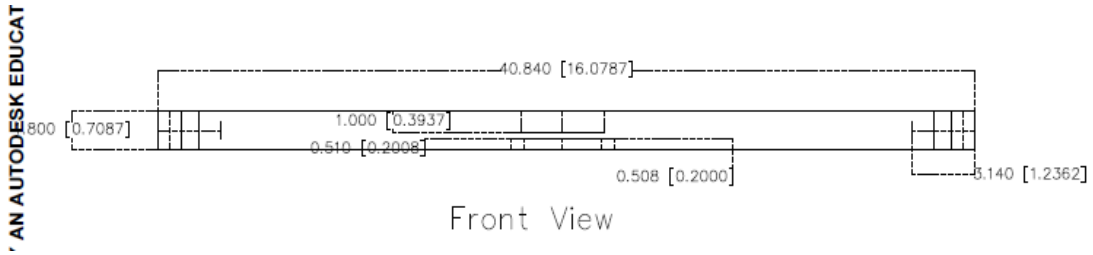

Figure 3-5. CAD drawing of the antenna adapter's front view is shown.

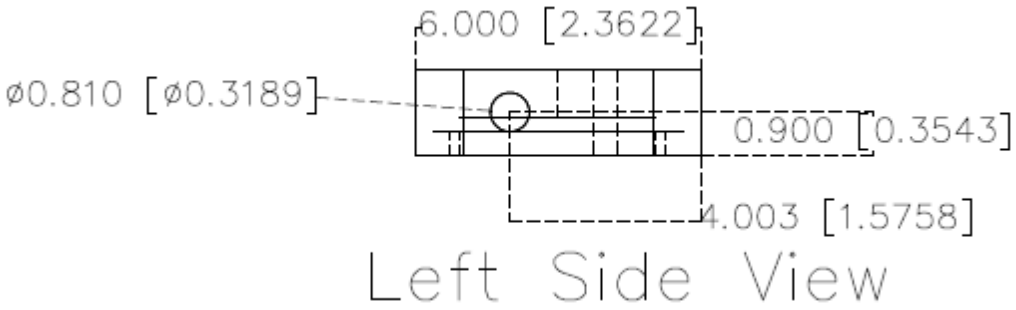

Figure 3-6. CAD drawing of the antenna adapter's side view is shown.

3.2.4 Horn Adapter Photographs

After the design in Auto CAD was completed, the drawings of the antenna bracket

were sent to the mechanic workshop for fabrication. The machined brackets fit well on the tower. Also, they could be rotated over the desired angles (±45°). The fabricated antenna adapters are shown in Figure 3-7. The MU GBIR system after fixing the horn antennas on the designed antenna brackets is shown in Figure 3-8.

a) 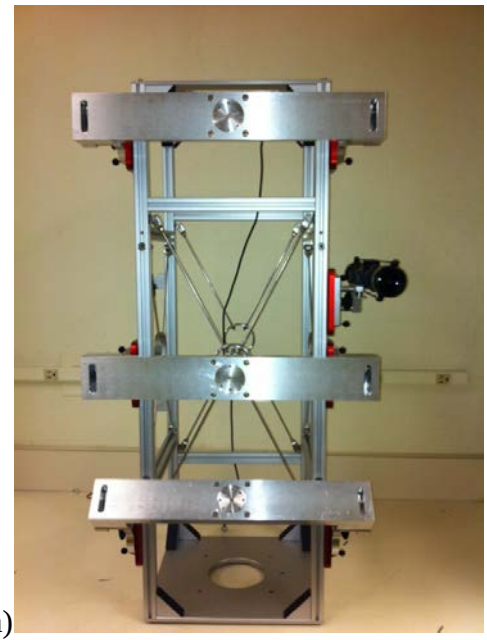 b) 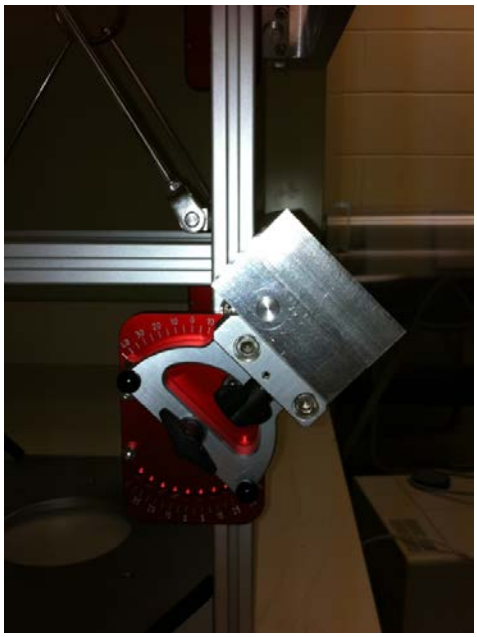

Figure 3-7. Photographs of the finished antenna adapters assembly are shown. a) Antenna adapters are shown on the tower (front view). b) Antenna adapters are shown on the tower (side view).

Figure 3-8. Photograph of the horn antennas mounted to the GBIR system is shown.

3.3 Trihedral Corner Reflectors

Several corner reflectors were designed and fabricated. TCRs with long side lengths of 12 inches and 39 inches were constructed. The corresponding maximum RCS values may be computed from equation 2.24 for each TCR and GBIR frequency as

Table 3-1. RCS values for various TCRs.

TCR Longest Side Length	C-band σ_{tcr}	Ku-band σ_{tcr}
~12 inches (~30 cm)	3 m^2	30 m^2
~39 inches (~1 m)	339 m^2	3440 m^2

One method of TCR fabrication used three triangular plates of aluminum (e.g. The 12 inch version is shown in Figures 3-9 and 3-10). In some cases, we may wish to use ten or more TCRS. In addition, we may have multiple experimental sites that may require leaving the TCR on site thus increasing the quantity needed.

A second TCR fabrication approach uses a lightweight base (e.g. cardboard or plastic) surrounded by aluminum foil. This approach's cost and production time may be very low. For example, a trihedral corner reflector with a longest edge of 12 inches may be made from a lightweight base material of size 12'' by 12''. Following the directions on Figure 3-11, each side of TCR base material may be formed. Aluminum foil is carefully applied to the base material to minimize surface ripples and seams. In the end, the surface deviations should be kept much smaller than the wavelength (e.g. C-band wavelength is about 5.6 cm. Ku-band wavelength is about 1.7 cm.). Figure 3-12 shows the completed TCR.

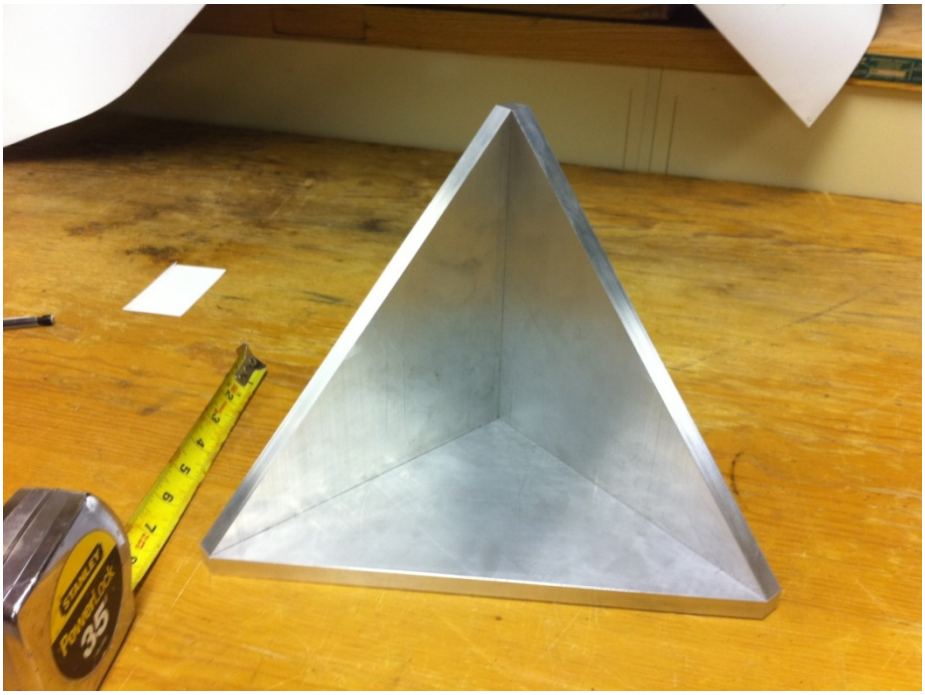

Figure 3-9. TCR using thick aluminum plates is shown (front view).

Figure 3-10. TCR using thick aluminum plates (one side shown). Hypotenuse is ~ 12".

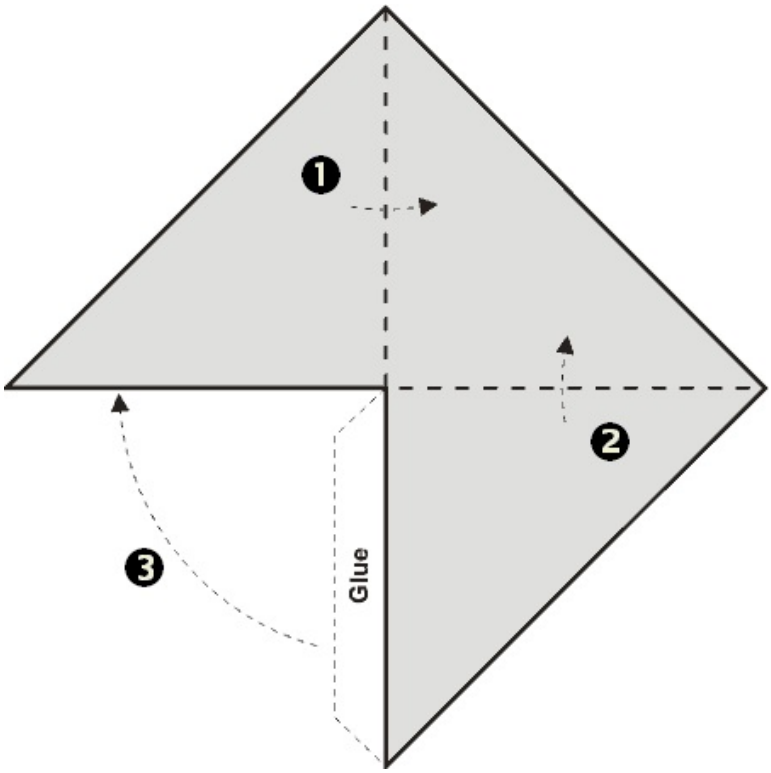

Figure 3-11. Diagram shows the steps for making a small TCR from a single sheet.

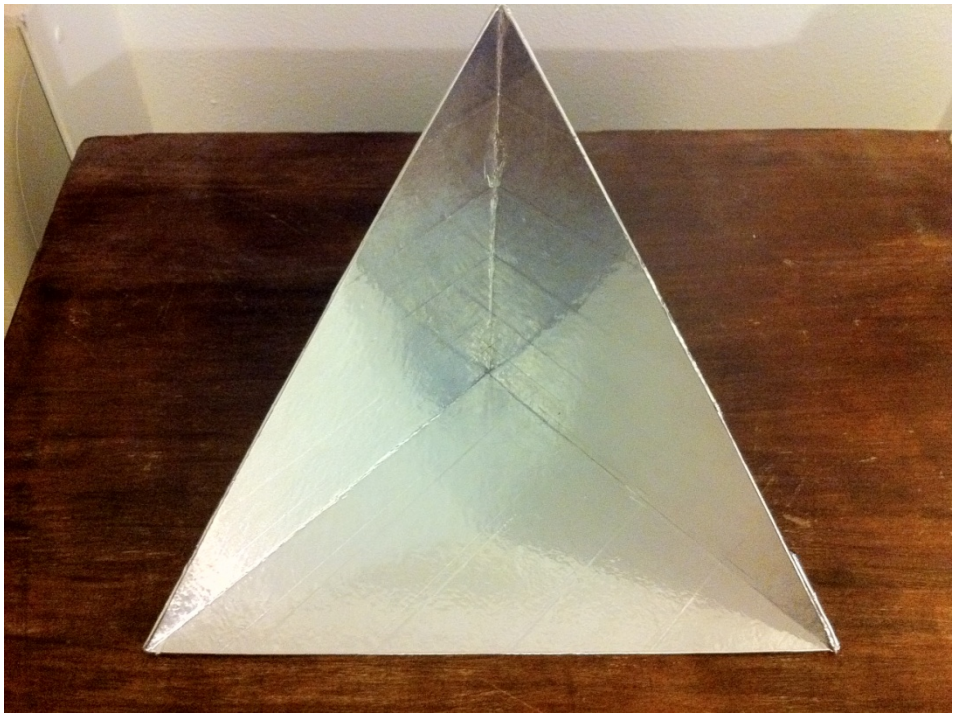

Figure 3-12. A low-cost TCR is shown.

Chapter 4. Field Sites Description

4.0 Introduction

This chapter focuses on the descriptions of four dam field sites where GBIR imagery were collected. In coordination with the United States Army Corps of Engineers (USACE), we gained access and information about several dams from the USACE regional office in Kansas City, Missouri. After site visits to many dams, we culled and prioritized our efforts to the four dams named Longview Dam, Blue Springs Dam, Tuttle Creek Dam, and Milford Dam (see Table 4-1). These sites were chosen because they offered an ideal test bed to calibrate the GBIR equipment. An overview of each of these dams is given in this chapter. The basic format of each overview is a) a brief narrative description, b) Google Earth views of each site, c) a plan view document of the site topography, land cover, monuments (e.g. experimental setup pins), and d) a photograph of each experimental setup pin.

Table 4-1. Field sites location and name is given.

Site Name	Nearby Location	Latitude	Longitude
Longview Dam	Lee's Summit, MO	38°55' N	94°28' W
Blue Springs Dam	Lee's Summit, MO	39°11' N	94°20' W
Tuttle Creek Dam	Manhattan, KS	39°15' N	96°35' W
Milford Dam	Junction City, KS	39°05' N	96°53' W

4.1 Longview Dam

4.1.1 Site information

The measurement of this dam focuses on Longview Dam Intake Tower Tilting and embankment movement. USACE does monitor various conditions at this dam. Monitoring of the tower is currently performed with tilt plate devices. Embankment movement is monitored with alignment monuments, crest centerline surveys, foundation settlement plates. Historical embankment movement was initially large (soft clay foundation), but movement has been relatively minimal in the last 10 yrs. The travel time by car to this site from Columbia, MO is about 2 hrs.

4.1.2 Site overview

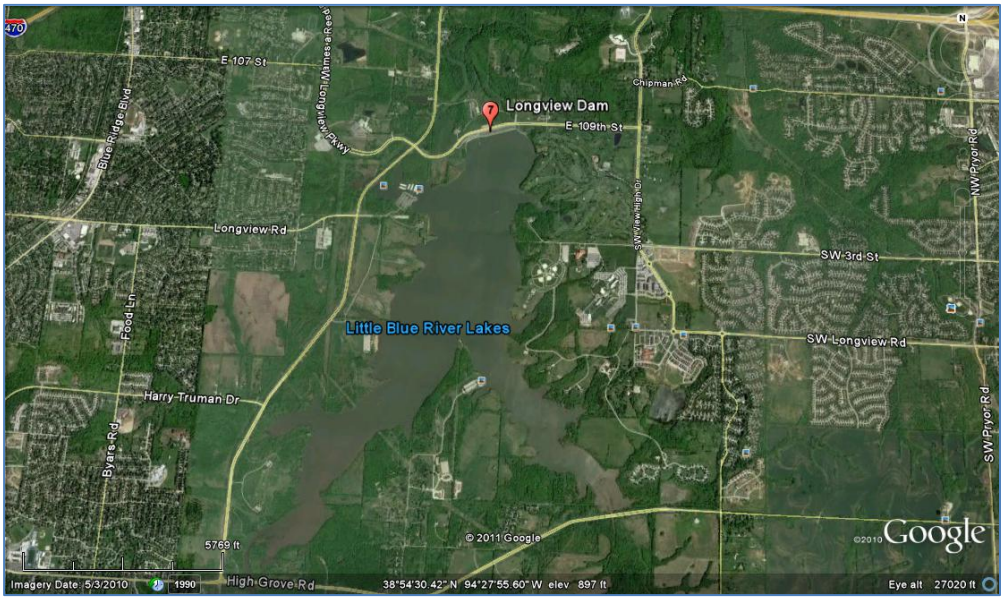

Figure 4-1.1. Google Earth view of Longview Dam is shown.

4.1.3 Site zoom

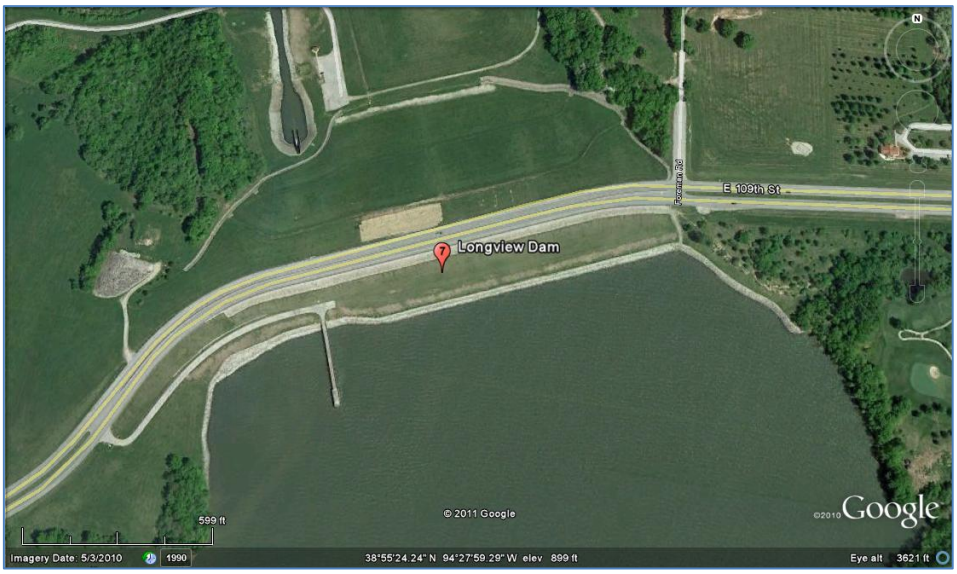

Figure 4-1.2. Google Earth zoomed-in view of Longview Dam is shown.

4.1.4 Site pins distribution

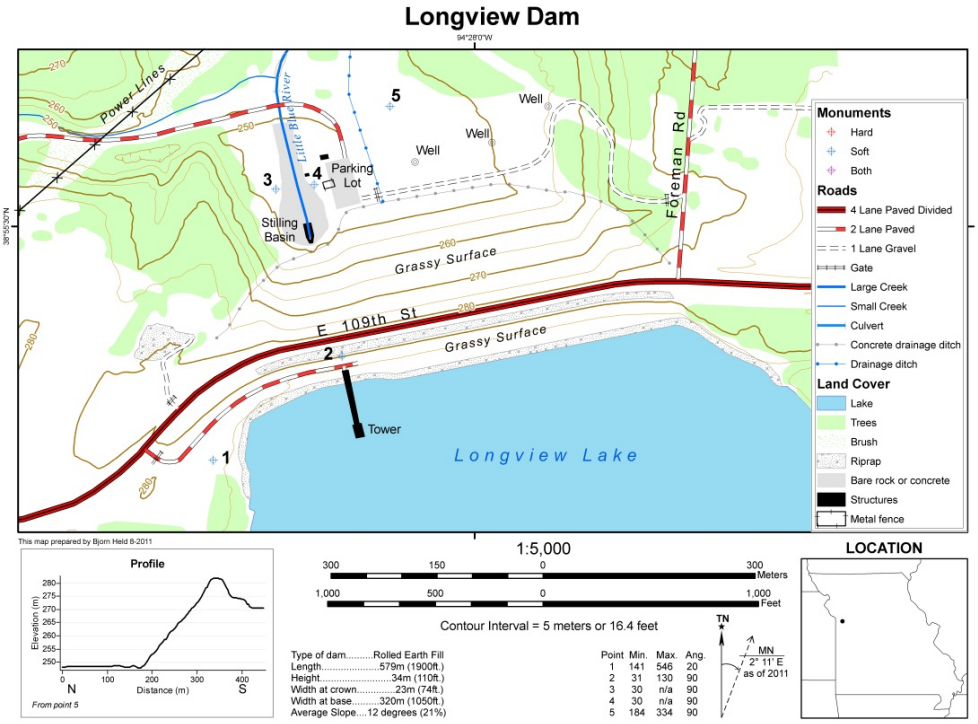

Figure 4-1.3. Site pins distribution at Longview Dam is illustrated.

4.1.5 Site pin photos

a) b) c)

d) e)

Figure 4-1.4. Photographs from each pin location at Longview Dam are presented. a) Pin 1, b) Pin 2, c) Pin 3, d) Pin 4, and e) Pin 5.

4.2 Blue Springs Dam

4.2.1 Site information

USACE measurements of Blue Springs Dam focus on the Intake Tower Tilting and embankment movement. Monitoring of the tower is currently performed with tiltplate devices. Embankment movement is monitored with alignment monuments, crest centerline surveys, foundation settlement plates. Historical embankment movement was initially large (soft clay foundation), but movement has been relatively minimal in the last 10 yrs. The travel time by car to this site from Columbia, MO is about 2 hours.

4.2.2 Site overview

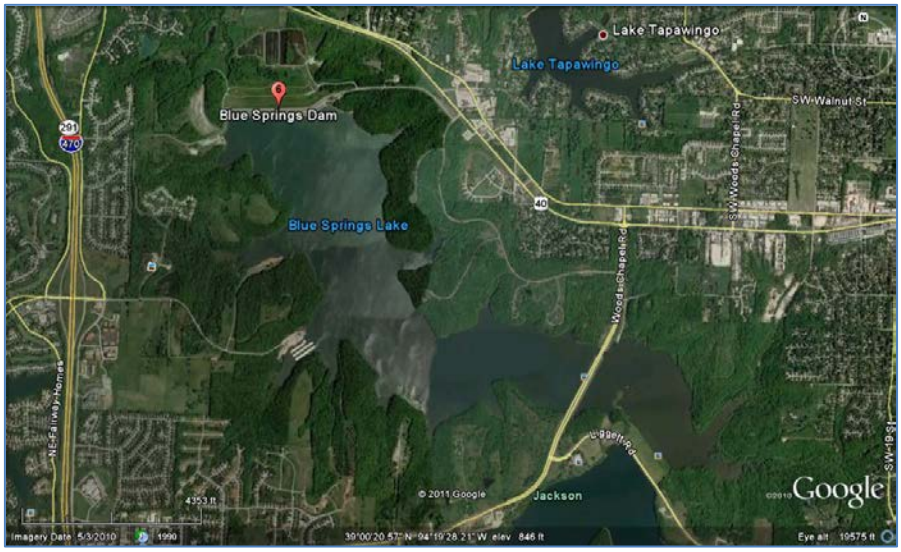

Figure 4-2.1. Google Earth view of Blue Springs Dam is shown.

4.2.3 Site zoom

Figure 4-2.2. Google Earth zoomed-in view of Blue Springs Dam is shown.

4.2.4 Site pins distribution

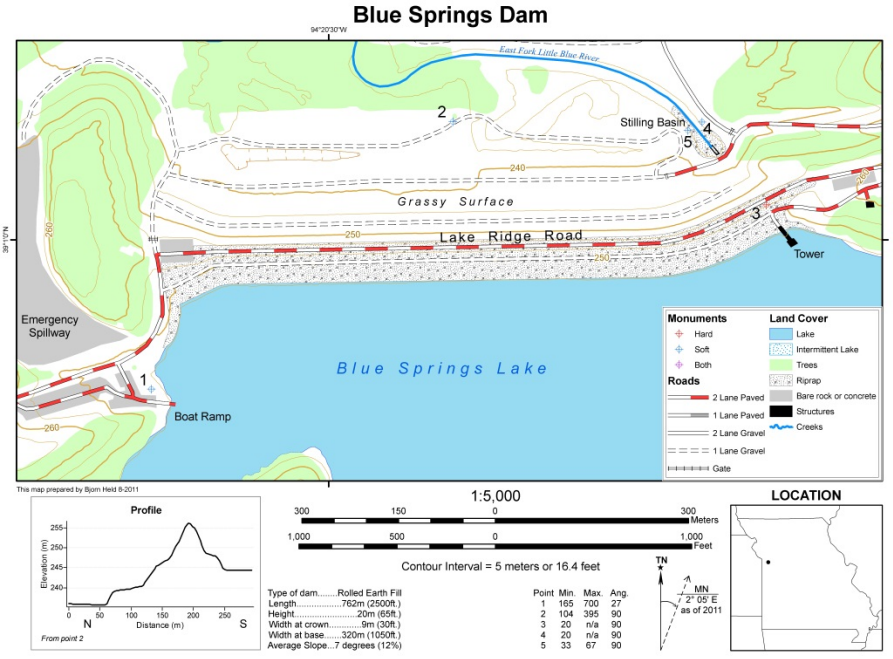

Figure 4-2.3. Site pins distribution at Blue Springs Dam is shown.

4.2.5 Site pin photos

a) b)

c) d)

e)

Figure 4-2.4. Photographs from each pin location at Blue Springs Dam are presented. a) Pin 1, b) Pin 2, c) Pin 3, d) Pin 4, and e) Pin 5.

4.3 Tuttle Creek Dam

4.3.1 Site information

The USACE measurement of Tuttle Creek Dam focuses on the Tuttle Creek spillway training wall. Existing structure joints are monitored by the USACE. The travel time to that site from Columbia, MO is about a 4 hour drive.

4.3.2 Site overview

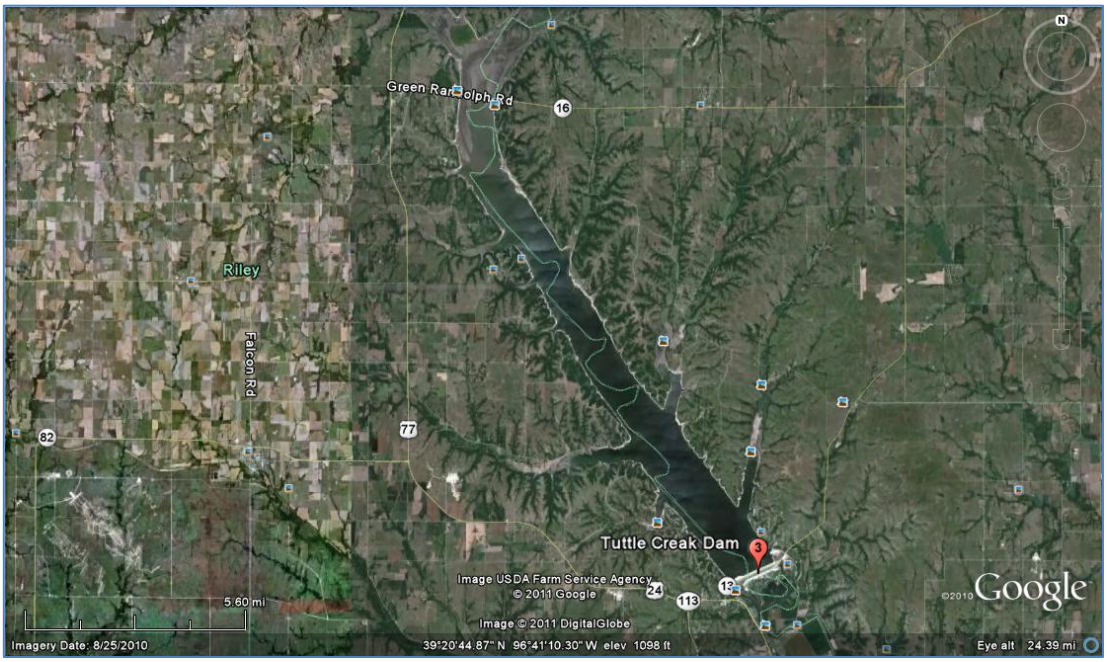

Figure 4-3.1. Google Earth view of Tuttle Creek Dam is shown.

4.3.3 Site zoom

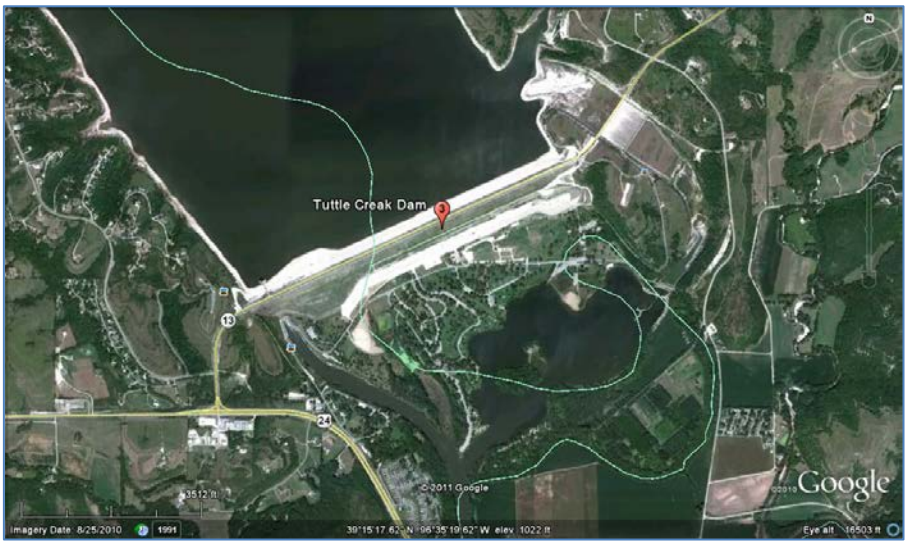

Figure 4-3.2. Google Earth zoomed-in view of Tuttle Creek Dam is shown.

4.3.4 Site pins distribution

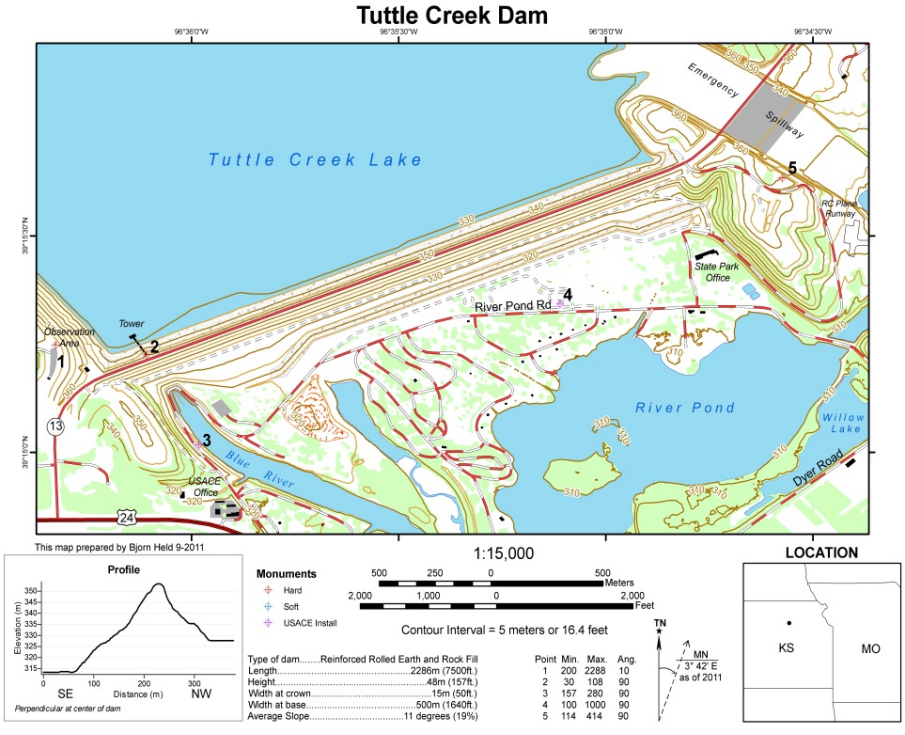

Figure 4-3.3. Site pins distribution at Tuttle Creek Dam is shown.

4.3.5 Site pin photos

a) b)

c) d)

e)

Figure 4-3.4. Photographs from each pin location at Tuttle Creek Dam are presented. a) Pin 1, b) Pin 2, c) Pin 3, d) Pin 4, and e) Pin 5.

4.4 Milford Dam

4.4.1 Site information

The USACE measurements of Milford Dam focus on the Milford Stilling Basin walls. Wall deflections are measured by the USACE at the headwall. Travel time by car to this site from Columbia, MO is about 4 hours (near Tuttle Creek Dam).

4.4.2 Site overview

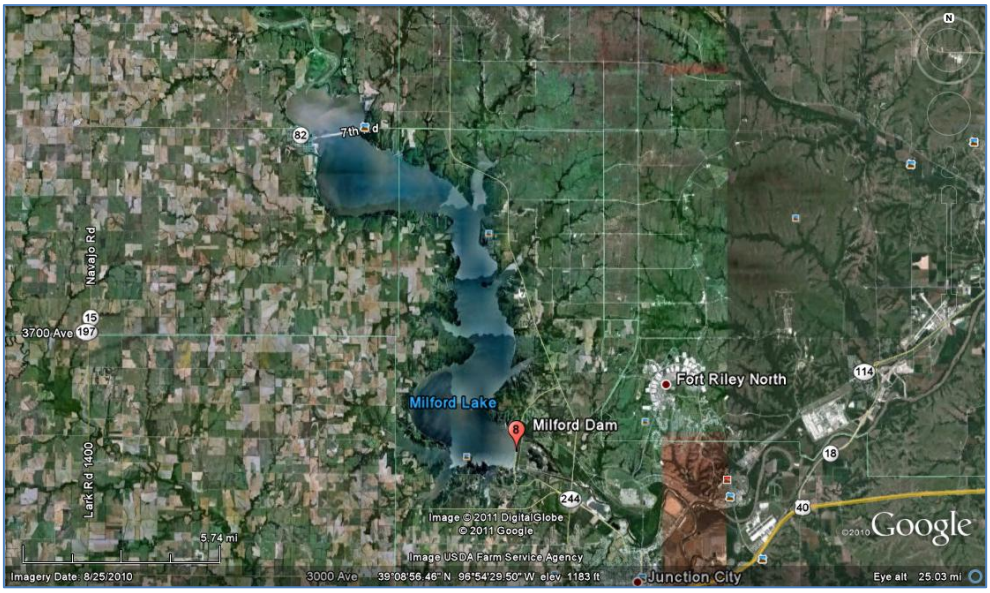

Figure 4-4.1. Google Earth view of Milford Dam is shown.

4.4.3 Site zoom

Figure 4-4.2. Google Earth zoomed-in view of Milford Dam is shown.

4.4.4 Site pins distribution

Figure 4-4.3. Site pins distribution at Milford Dam is illustrated.

4.4.5 Site pin photos

a)

b)

c)

Figure 4-4.4. Photographs from each pin location at Milford Dam are presented. a) Pin 1, b) Pin 3, and c) Pin 5.

Chapter 5. GBIR Imagery from Field Sites

5.1 Introduction

Various GBIR image products were generated for each study site: Longview Dam, Blue Springs Dam, Tuttle Creek Dam, and Milford Dam as described in Chapter 4. For each image, the decimation factor *D* is listed in Appendix B. Intensity images in polar and rectangular coordinates systems are generated for each site. The excellent imaging capability can be seen in the images presented in this chapter. Initial interferometric products are presented for a number of sites. The initial interferometric products show clear phase ramps and agree well with initial expectations.

Different color bands in the interferogram correspond to different phase delays between the received echoes. If the imaged scene is correlated or coherent to the RADAR, clear continuous color bands or cycles could be observed in the interferogram. Instead, if the imaged scene is decorrelated or incoherent to the RADAR, the interferogram may display random color speckles.

For the single pass interferogram, the phase delay between the echoes to the upper and lower receiver is caused mainly by the base-line offset between the two receiving antennas. The color cycles (i.e. phase ramps) observed in the single pass

interferogram correspond to the topographic phase delays. For the repeat pass interferogram, the phase ramps are caused by the combined effects of atmosphere, deformation and noise. Hence, from the initial repeat pass interferogram, no clear information of the deformation could be obtained. However, after eliminating the atmospheric effects and applying certain methods (e.g. filtering, phase unwrapping, stacking) to reduce the noise in the initial interferograms, the deformation of the scene could be obtained from the final unwrapped interferogram. In the final interferogram, the color bands represent the phase difference caused only by the deformation of the imaged scene. The deformation is directly related to the interferometric phase difference. For C-band operation, if we set the whole color cycle to a phase difference of 2π, then the whole color cycle corresponds to a deformation of about 28 mm [Hanssen, 2001]. For Ku-band operation, if we set the whole color cycle to a phase difference of 2π, then the whole color cycle corresponds to a deformation of about 8.7 mm.

5.2 Image processing results of Longview Dam

5.2.1 Pin 1 at Longview Dam

Pin 1 at Longview Dam is the site where we placed the GBIR to scan the front face of the Longview Lake Dam, including the tower. At this site, the Ku-band 2-m antenna

was utilized. Figure 5-2.1 and Figure 5-2.2 show the multi-look intensity (MLI) images in polar and rectangular coordinates generated from the raw data collected at this site on 02/17/2012. The maximum distance from the radar to the dam is about 550 m. From Figure 5-2.2, the intensity of the back-scattered echo from the dam's face is observed. The bright strip in this image is the dam's face and that beyond the farther end of the dam is the vegetation. The tower in the water area and the bridge to the tower are observed as well. Note that saturation occurs at the bridge area in the image since part of the bridge surface is covered by strong metallic scatterers. The two bright dots in front of bridge stand correspond to two metal posts in the water.

Figure 5-2.3 is the interferogram generated from a single pass scan on 02/18/2012. Two single look complex (SLC) images from the upper and lower antennas are co-registered and multi-looked to make the interferogram. Different colors in this interferogram represent different phase delays of the echoes received by the upper and lower antennas, respectively. The phase ramp indicates the target remains coherent during the scan.

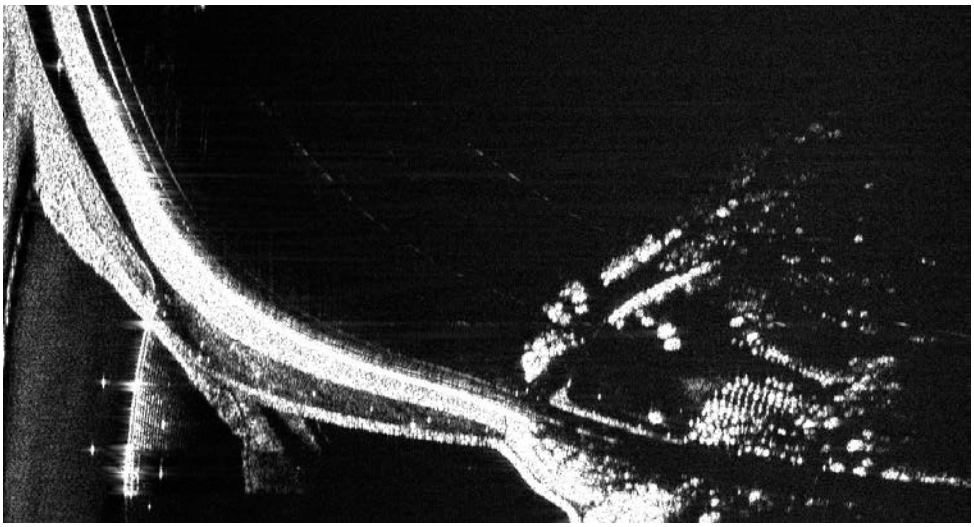

Figure 5-2.1. Ku-band MLI image in radar coordinates for Pin 1 at Longview Dam on 02/17/2012 is shown. The 2-m antenna is used.

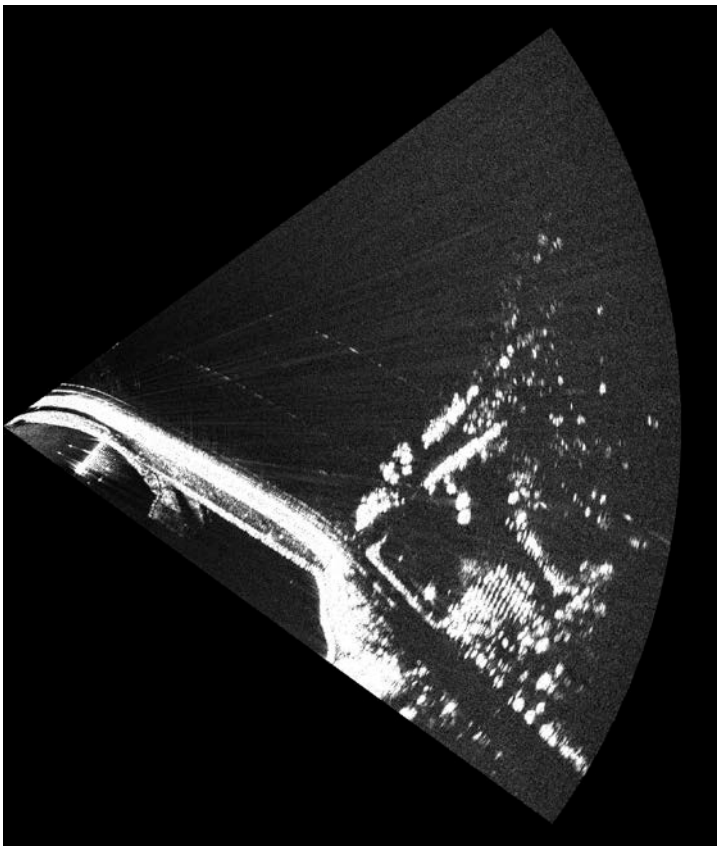

Figure 5-2.2. Ku-band MLI image in rectangular coordinates for Pin 1 at Longview Dam on 02/17/2012 is shown. The 2-m antenna is used.

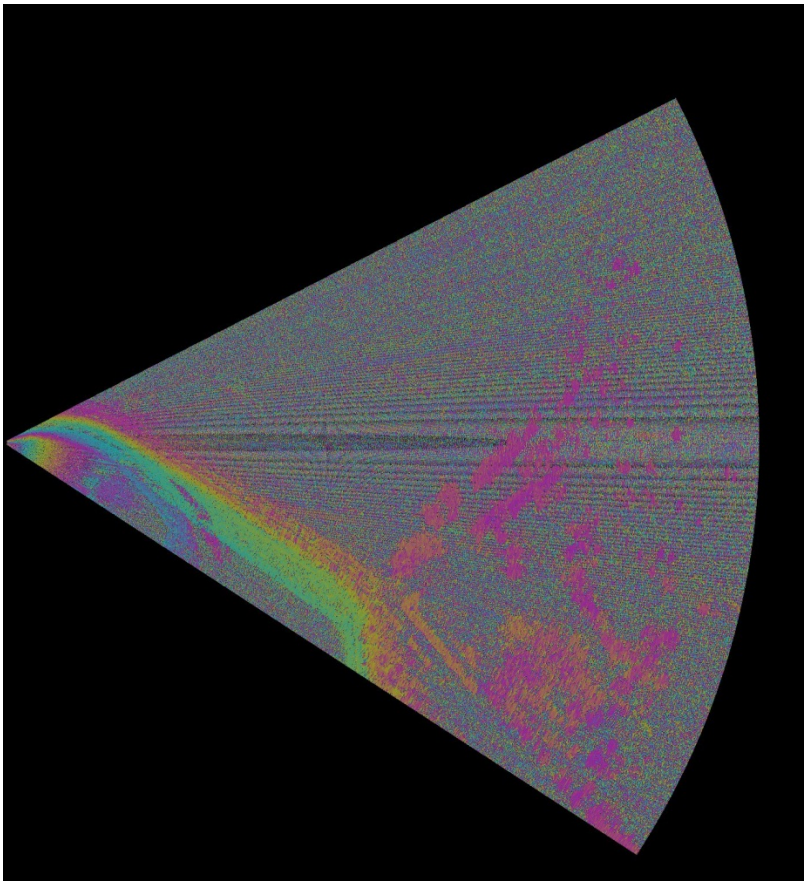

Figure 5-2.3. Ku-band single pass interferogram for Pin 1 at Longview Dam on 02/17/2012 is shown. The 2-m antenna is used.

5.2.2 Pin 3 at Longview Dam

Pin 3 is the site to the northwest of the stilling basin where the GBIR was placed to monitor the displacement of the wall of the spillway. At this site, the Ku-band horn antenna was applied since the distance from the radar to the target is around 50 m, which is less than the far field beginning range of the 2-m antenna (~500 m at Ku-band). Figure 5-2.4 is the MLI image in polar coordinates generated from the data collected at this site. The range resolution for Ku-band is about 0.75 m. However, the azimuth beam width for the horn antenna is about 10°, which means the azimuth pixel size is larger

than for the 2-m antenna (e.g. about 9 m at 50 m for the horn antenna, and about 0.44 m at 50m for the 2-m antenna). The MLI image at this site corresponds to the larger azimuth pixel size and reduced number of azimuth pixels for the near imaging of the spillway area. Figure 5-2.5 is the MLI image in rectangular coordinates with 201 × 171 pixels. We can observe the bright area which corresponds to the spillway from about 70^{th} pixel to 90^{th} pixel in range (i.e. about 50m in range, which corresponds well with the physical distance between the radar and the spillway).

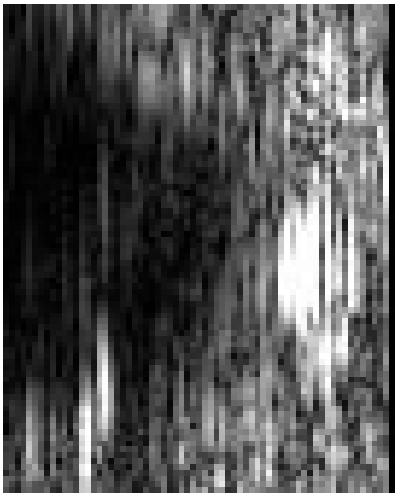

Figure 5-2.4. Ku-band MLI image in radar coordinates for Pin 3 at Longview Dam on 08/02/2011 is shown. The horn antenna is used.

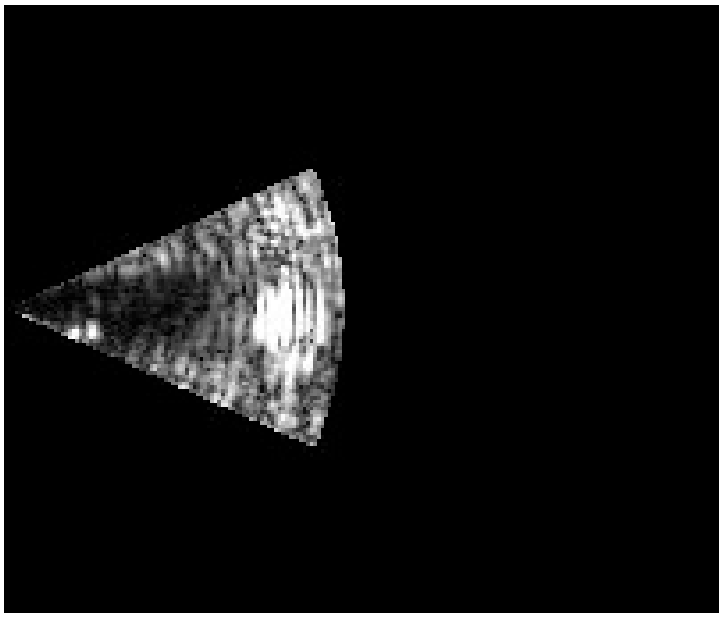

Figure 5-2.5. Ku-band MLI image in rectangular coordinates for Pin 3 at Longview Dam on 08/02/2011 is shown. The horn antenna is used.

5.2.3 Pin 4 at Longview Dam

The GBIR is placed to monitor the displacement of the wall of the spillway at Pin 4, which is the site to the northeast of the stilling basin. The distance from Pin 4 to the spillway is around 55 m. Experimental details are similar to those for Pin 3. Figure 5-2.6 and Figure 5-2.7 are the MLI images generated from the data collected on 08/01/2011 in polar coordinates and rectangular coordinates, respectively. The bright region in Figure 5-2.7 is observed as the wall of the spillway.

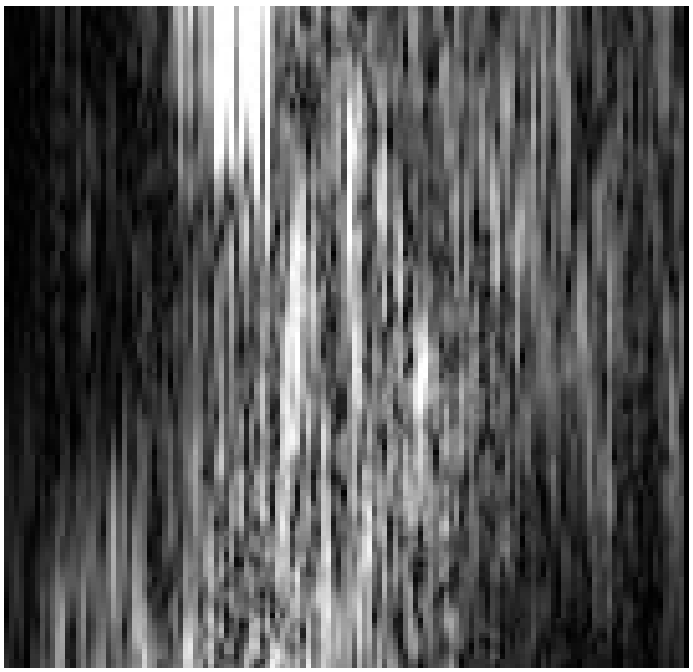

Figure 5-2.6. Ku-band MLI image in radar coordinates for Pin 4 at Longview Dam on 08/01/2011. The horn antenna is used.

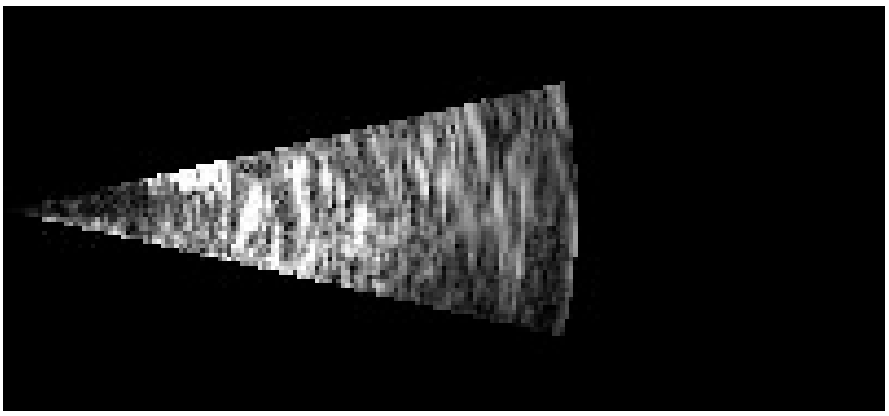

Figure 5-2.7. Ku-band MLI image in rectangular coordinates for Pin 4 at Longview Dam on 08/01/2011. The horn antenna is used.

5.2.4 Pin 5 at Longview Dam

At Pin 5, the GBIR is placed to scan the back face of Longview Dam. At this site, Ku-band 2-m antenna was utilized. The distance from the radar to the center of the dam is about 185 m. Figure 5-2.8 and Figure 5-2.9 are MLI images generated from the data

collected at Pin 5 on 08/02/2011 in polar and rectangular coordinates, respectively. The road tracks at the back face of the dam are observed in the imagery. Figure 5-2.10 shows a single pass interferogram for this site on 08/02/2011. The clear phase ramp indicates the phase difference between the echoes received by the upper and lower antennas. The dam and nearby area in the scene are coherent during this scan.

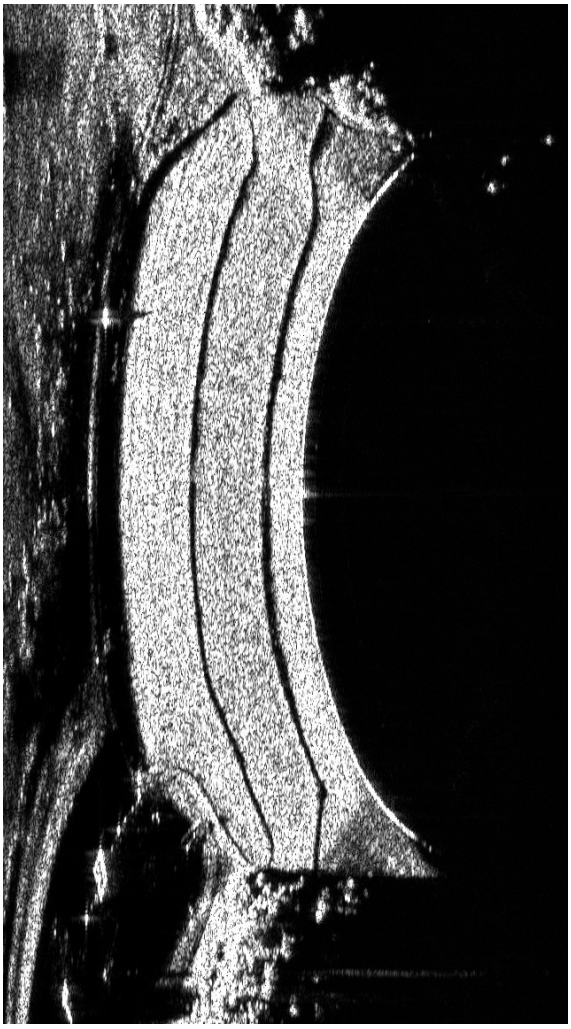

Figure 5-2.8. Ku-band MLI image in radar coordinates for Pin 5 at Longview Dam on 08/02/2011 is shown. The 2-m antenna is used.

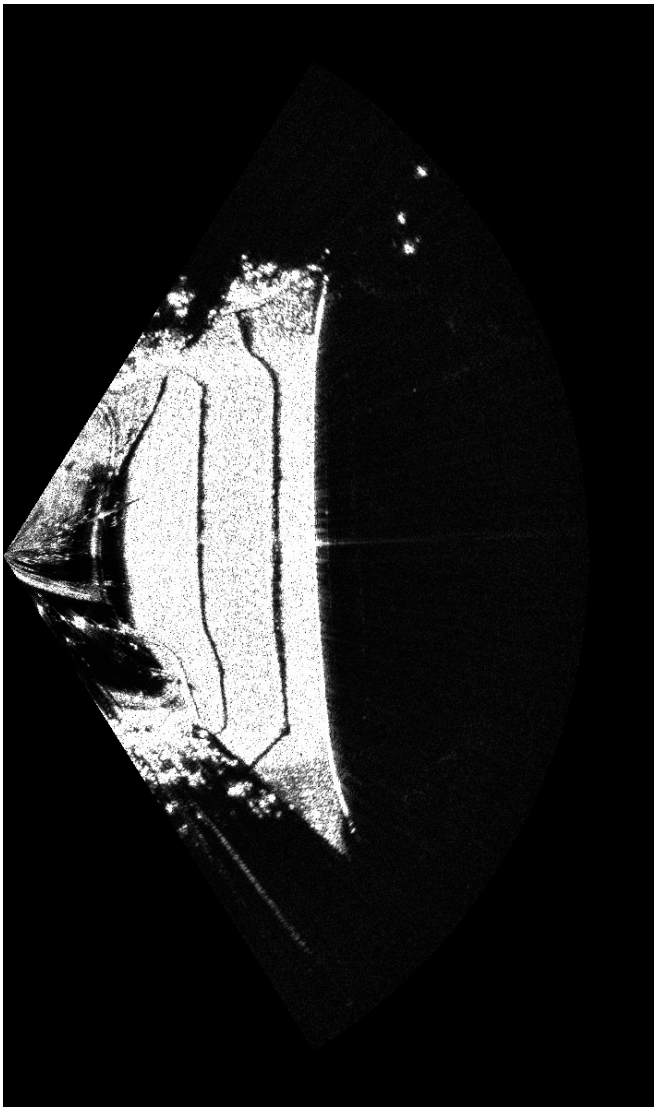

Figure 5-2.9. Ku-band MLI image in rectangular coordinates for Pin 5 at Longview Dam on 08/02/2011 is shown. The 2-m antenna is used.

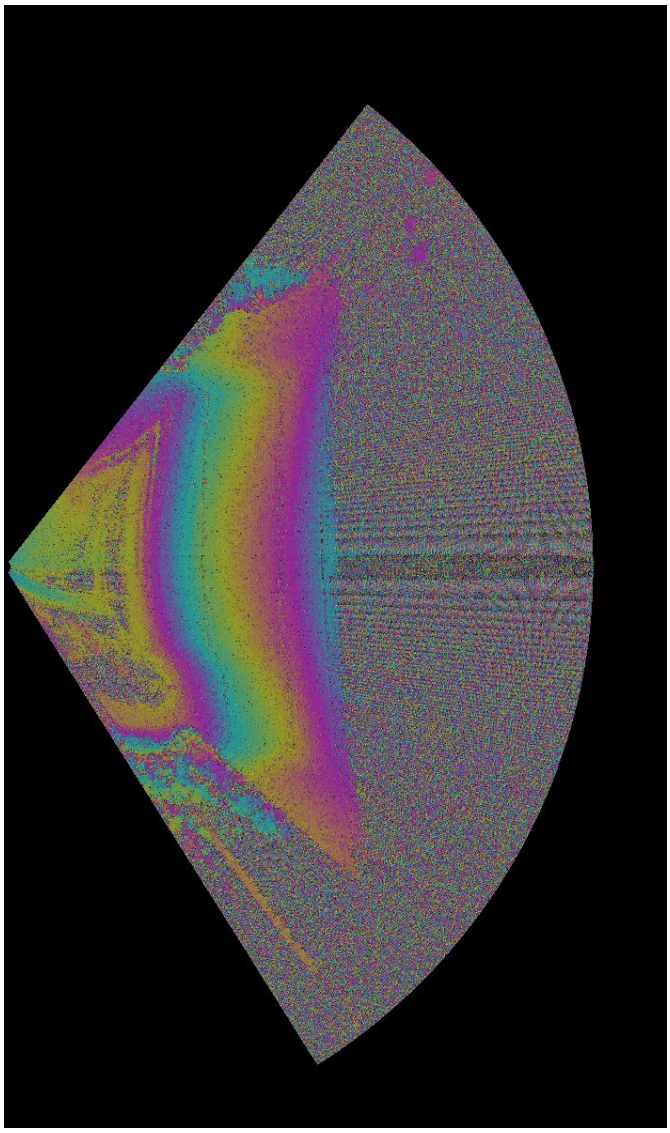

Figure 5-2.10. Ku-band single pass interferogram for Pin 5 at Longview Dam on 08/02/2011 is shown. The 2-m antenna is used.

5.3 Image processing results of Blue Springs Dam

5.3.1 Pin 2 at Blue Springs Dam

At Pin 2 for the Blue Spring dam, the GBIR scans the back face of the dam. The distance from Pin 2 to the farthest end of the dam is about 400 m. C-band fully polarized data has been collected at this site. C-band fully polarized MLI images (HH,

VH, HV, VV) are presented in Figure 5-3 (a)-(d). From each image, bright return strips are observed corresponding to part of the back face of the dam. Also, some shadow behind the bright strips occurs because of the steep ramp at the back face of the dam. Those bright dots correspond to metal posts near the earthen slope leading up to the dam. The co-polarized MLI images (HH, VV) have a slightly stronger intensity than the cross-polarized MLI images (VH, HV).

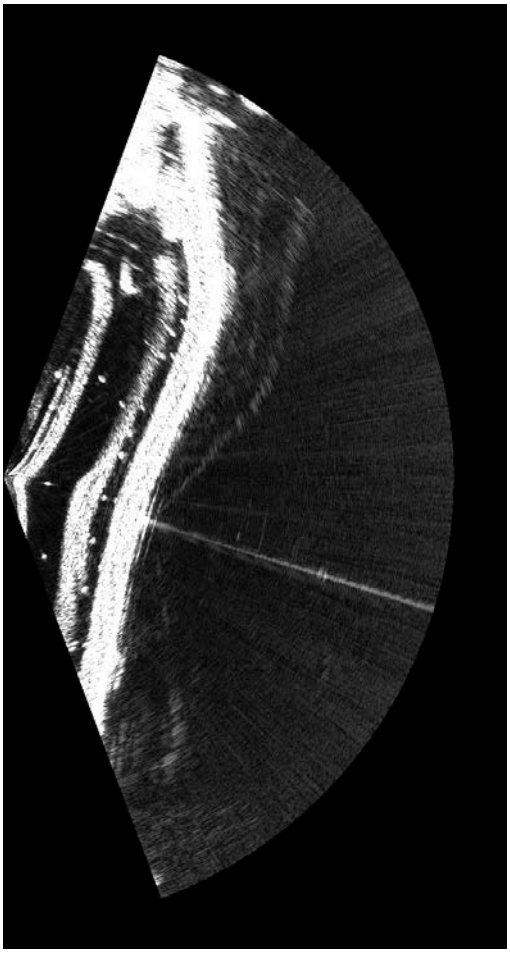

Figure 5-3(a). C-band (HH) MLI image in rectangular coordinates for Pin 2 at Blue Springs Dam on 02/18/2012 is shown. The 2-m antenna is used.

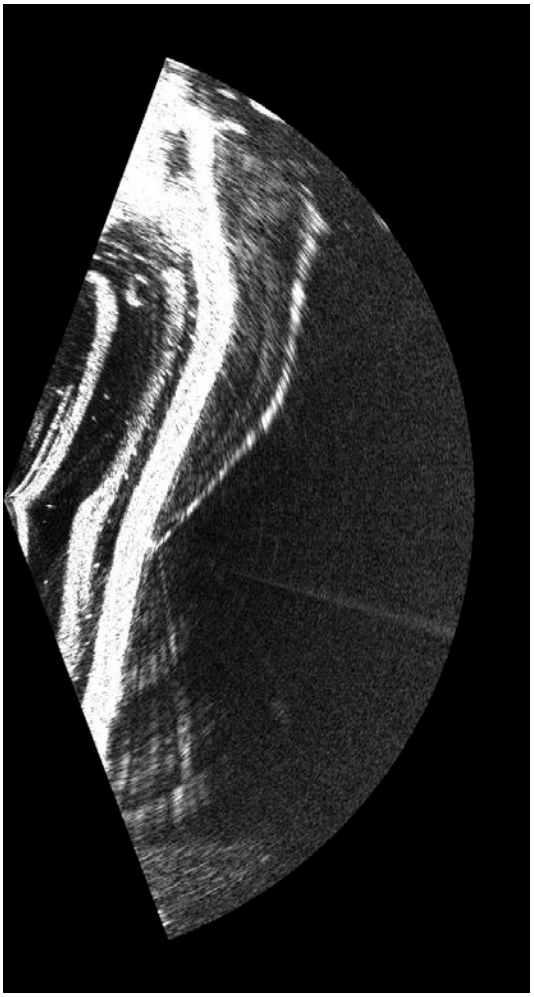

Figure 5-3(b). C-band (VH) MLI image in rectangular coordinates for Pin 2 at Blue Springs Dam on 02/18/2012 is shown. The 2-m antenna is used.

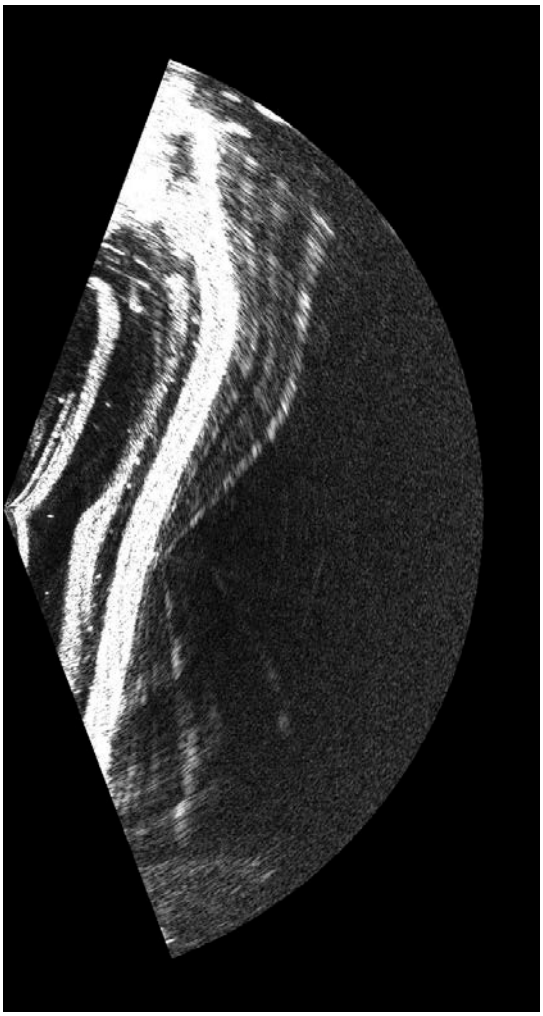

Figure 5-3(c). C-band (HV) MLI image in rectangular coordinates for Pin 2 at Blue Springs Dam on 02/18/2012 is shown. The 2-m antenna is used.

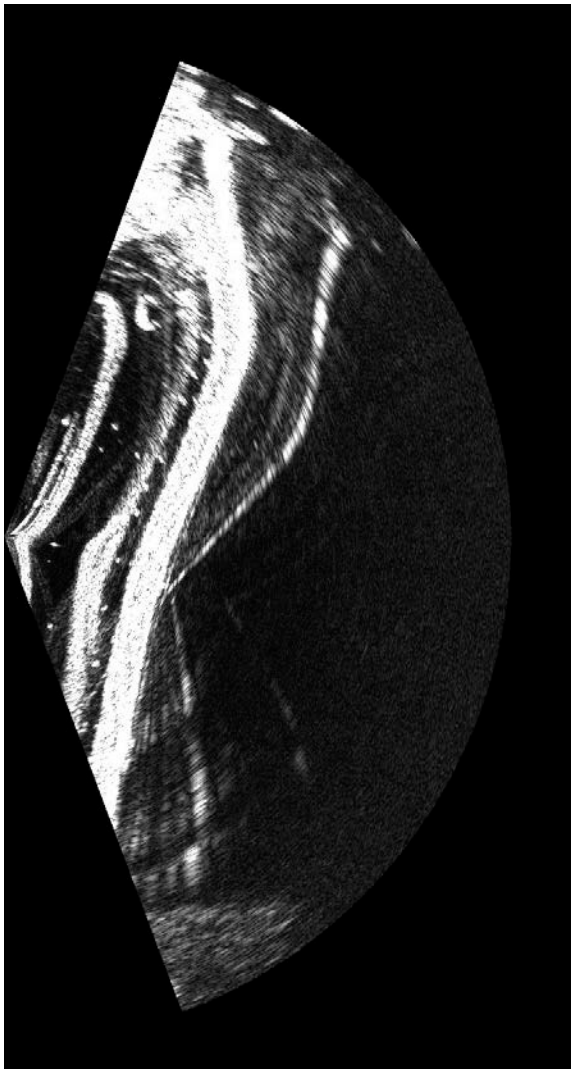

Figure 5-3(d). C-band (VV) MLI image in rectangular coordinates for Pin 2 at Blue Springs Dam on 02/18/2012 is shown. The 2-m antenna is used.

5.4 Image processing results of Tuttle Creek Dam

5.4.1 Pin 1 at Tuttle Creek Dam

At Pin 1, the GBIR scans the front face of Tuttle Creek Dam (including the tower). The maximum distance from the radar to the dam is about 2300 m. The Ku-band 2-m antenna was utilized for this site. Figure 5-4.1 and Figure 5-4.2 are the MLI images

generated from the data collected on 09/16/2011 in polar and rectangular coordinates, respectively. In Figure 5-4.2, the tower of the dam and the buoys on the water surface near the tower are observed. Also, the black strip on the right side of the tower corresponds to shadowing of the tower.

Figure 5-4.3 is a single pass interferogram for this site from the data collected on 09/16/2011. The phase ramp indicates the phase delay between the echoes to the upper and lower receiving antennas. Figure 5-4.4 shows the repeat pass interferogram generated from the data sets collected from September, 2011 and February, 2012. The image coregistration for these two different data sets was successful and the dam retained to be coherent in this interferogram.

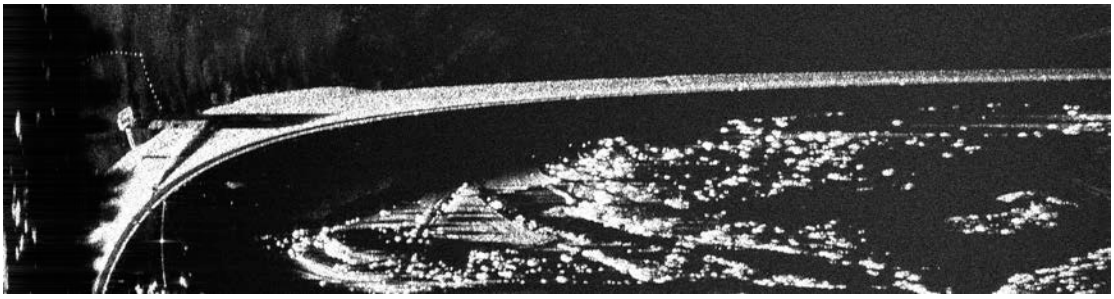

Figure 5-4.1. Ku-band MLI image in radar coordinates for Pin 1 at Tuttle Creek Dam on 09/16/2011 is shown. The 2-m antenna is used.

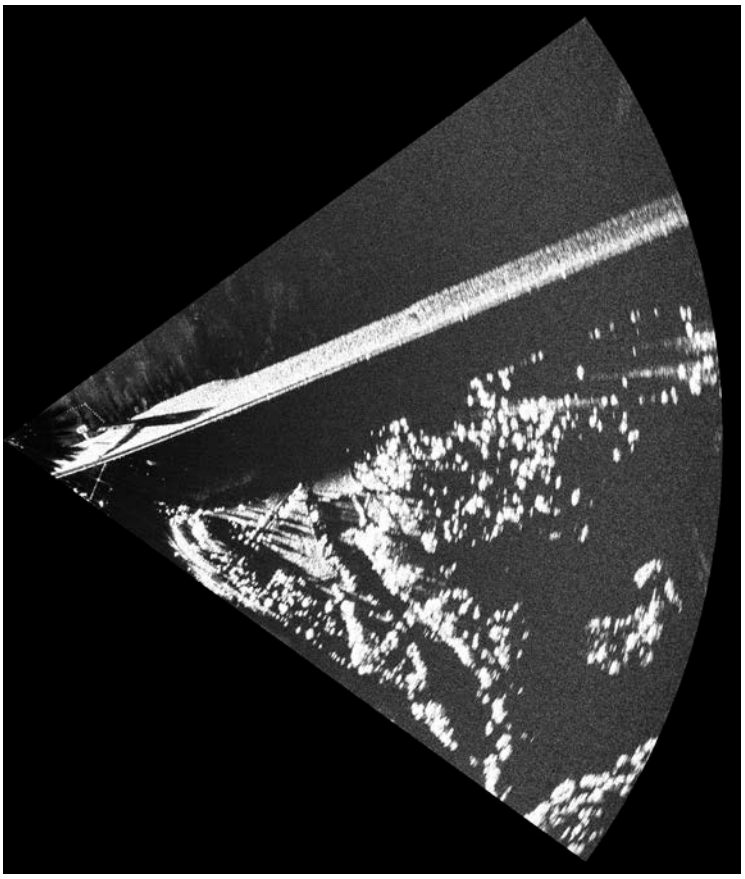

Figure 5-4.2. Ku-band MLI image in rectangular coordinates for Pin 1 at Tuttle Creek Dam on 09/16/2011 is shown. The 2-m antenna is used.

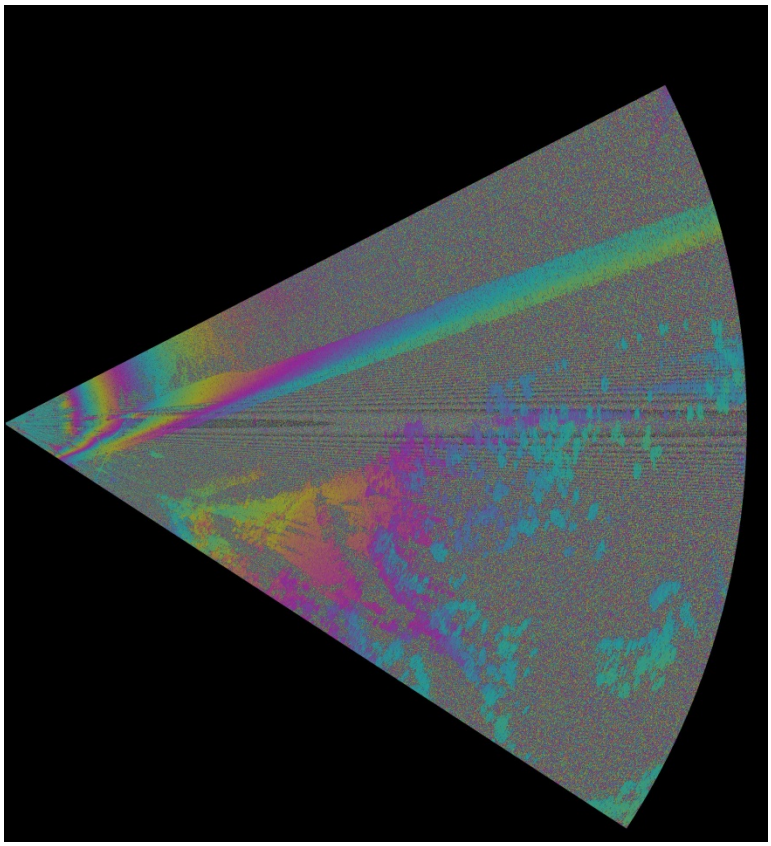

Figure 5-4.3. Ku-band single pass interferogram for Pin 1 at Tuttle Creek Dam on 09/16/2011 is shown. The 2-m antenna is used.

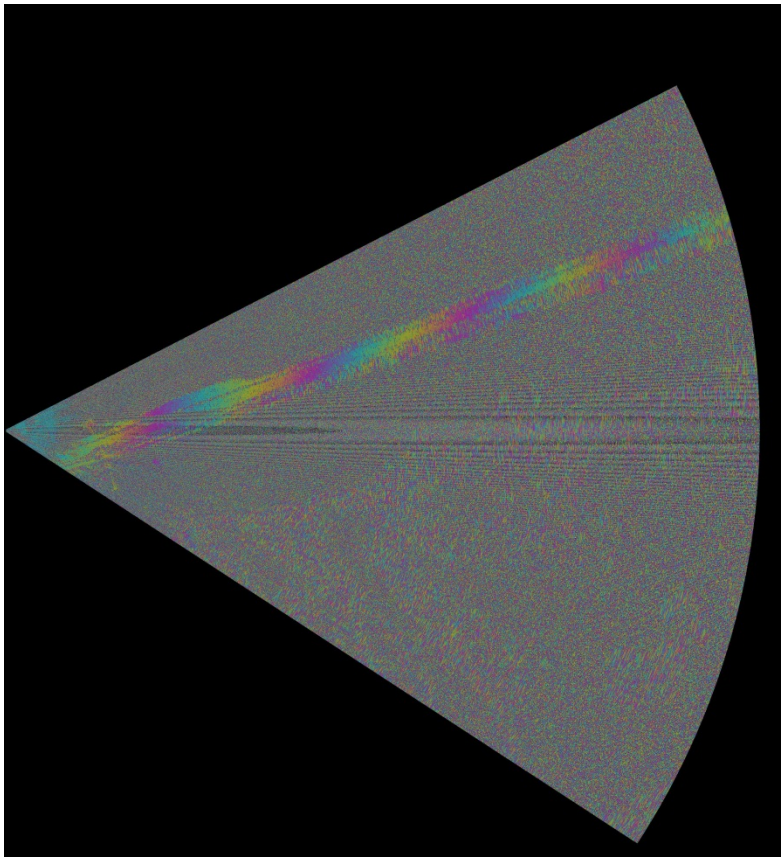

Figure 5-4.4. Ku-band repeat pass interferogram for Pin 1 at Tuttle Creek Dam on 09/16/2011-02/17/2012 is shown. The 2-m antenna is used.

5.4.2 Pin 5 at Tuttle Creek Dam

Pin 5 is the site where we placed the GBIR to scan the concrete apron at the emergency spillway at Tuttle Creek Dam. Ku-band 2-m antenna was applied at this site. The maximum distance from the radar to the apron is around 400m. Figure 5-4.5 and Figure 5-4.6 are the MLI images generated from the data collected at this site on 09/16/2011 in polar and rectangular coordinates, respectively. From Figure 5-4.6 we can see clearly some saturation occurs at the bright strip due to the metal gates at the bridge above the spillway. Also, next to the metal gates there is a quad area which looks

a little dimmer. That's the concrete apron we tried to scan. Figure 5-4.7 is the single pass interferogram generated from the data collected on 09/16/2011. The clear color cycle in this image represents different phase delay of the echoes received by the upper and lower receivers, respectively. A repeat pass interferogram shown in Figure 5-4.8 is generated from the first scan and the last scan of a one-day time-series scans. The one-day repeat pass interferogram shows that the scene monitored was coherent.

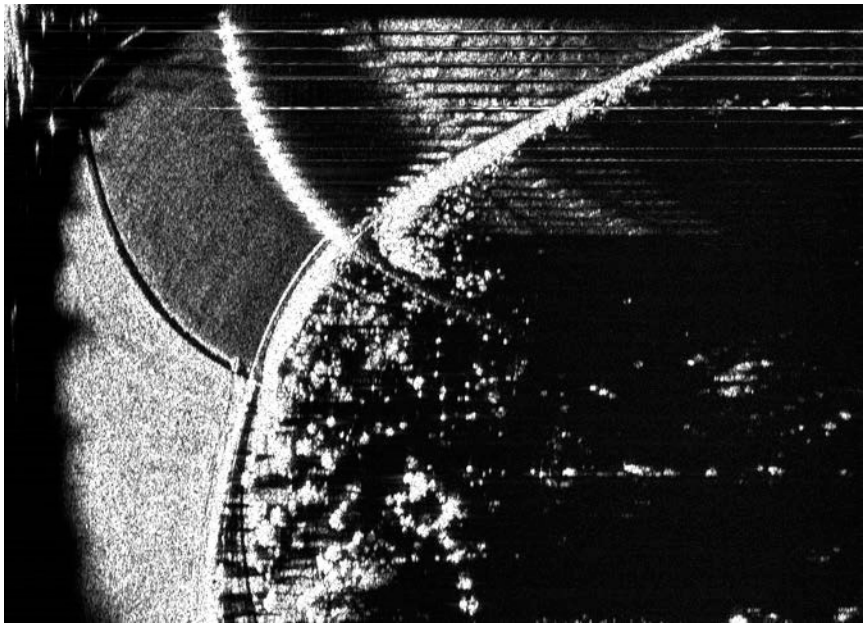

Figure 5-4.5. Ku-band MLI image in radar coordinates for Pin 5 at Tuttle Creek Dam on 09/16/2011 is shown. The 2-m antenna is used.

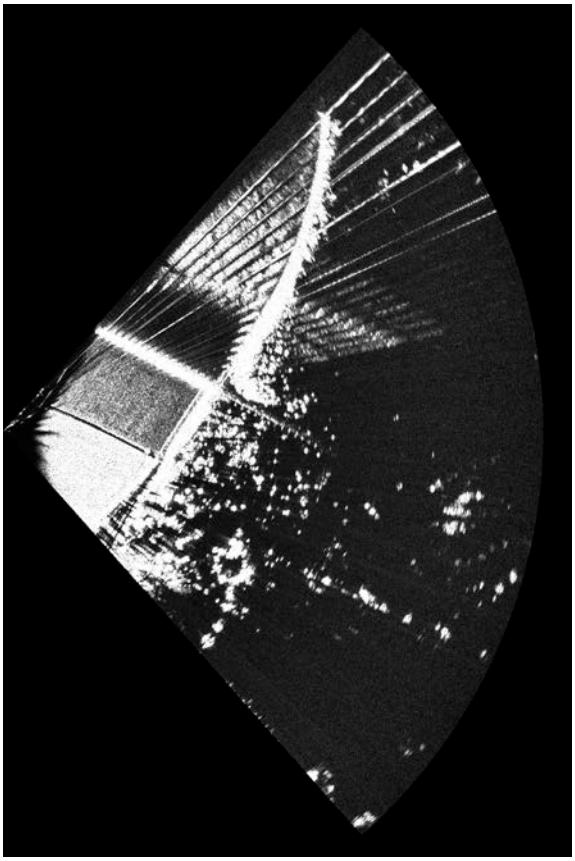

Figure 5-4.6. Ku-band MLI image in rectangular coordinates for Pin 5 at Tuttle Creek Dam on 09/16/2011 is shown. The 2-m antenna is used.

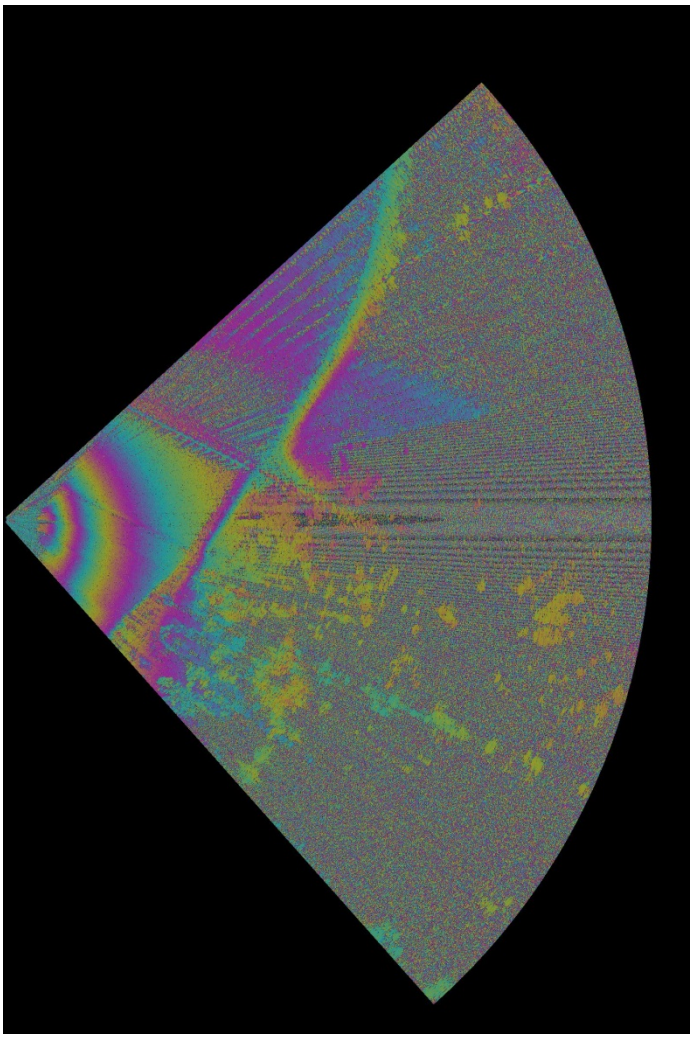

Figure 5-4.7. Ku-band single pass interferogram for Pin 5 at Tuttle Creek Dam on 09/16/2011 is shown. The 2-m antenna is used.

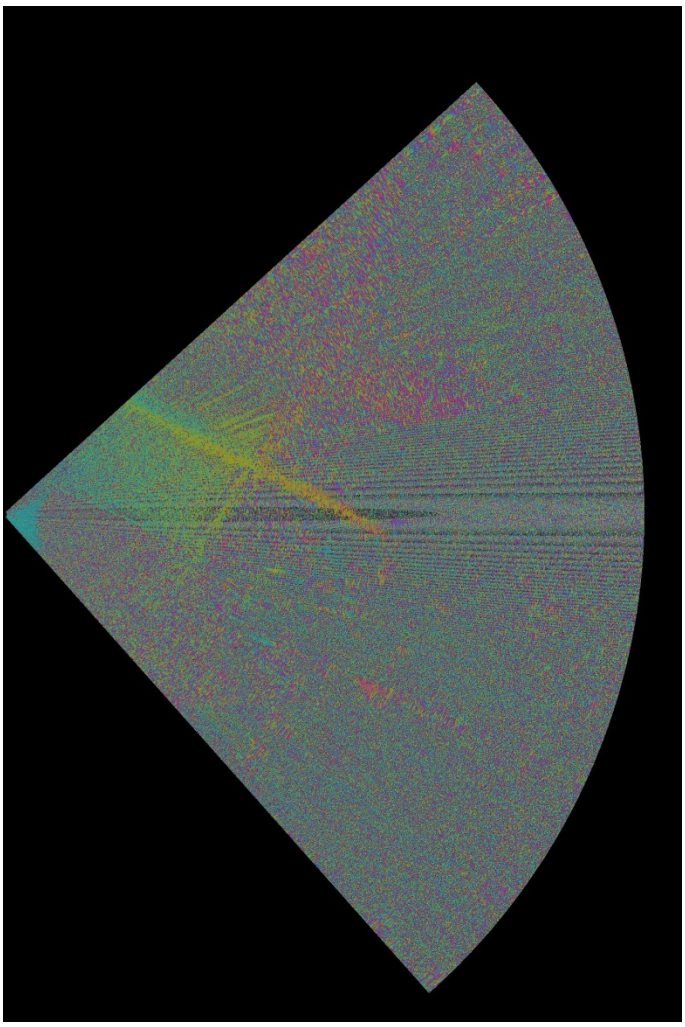

Figure 5-4.8. Ku-band one day repeat pass interferogram for Pin 5 at Tuttle Creek Dam on 09/16/2011 is shown. The 2-m antenna is used.

5.5 Image processing results of Milford Dam

5.5.1 Pin 1 at Milford Dam

At Milford Dam Pin 1, the GBIR scans the riprap covered front face (upstream side) of the dam. Both Ku-band and C-band 2-m antennas were utilized at this site. The maximum distance from the radar to the dam is about 1800 m. Figure 5-5.1 and Figure 5-5.2 are the MLI images generated from the data collected at this site on 09/16/2011 in

polar and rectangular coordinates. The dam as well as some vegetation at the farther end of the dam are observed in the image as shown in Figure 5-5.2.

Figure 5-5.3 is a Ku-band single pass interferogram from one scan on 09/16/2011. Coherence of the dam is maintained during this scan. Figure 5-5.4 shows a Ku-band repeat pass interferogram from data sets collected in September, 2011 and February, 2012. The co-registration of images from the two data sets is not that good but still acceptable. From this coherent interferogram, phase ramps are observed.

Figure 5-5.5 shows a C-band repeat pass interferogram with single polarization (HH) configuration from data sets collected in November, 2011 and February, 2012. The co-registration of images went well and the high coherence of the dam could be quantitatively observed from this image. Also, the side lobes of the antenna beam generate a few image artifacts on each side of the dam.

Figure 5-5.1. Ku-band MLI image in rectangular coordinates for Pin 1 at Milford Dam on 09/16/2011 is shown. The 2-m antenna is used.

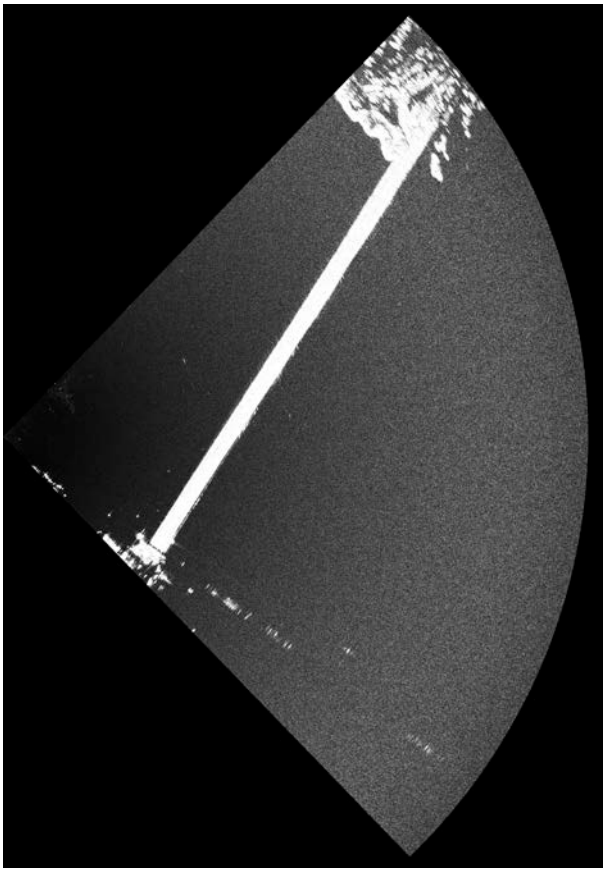

Figure 5-5.2. Ku-band MLI image in rectangular coordinates for Pin 1 at Milford Dam on 09/16/2011 is shown. The 2-m antenna is used.

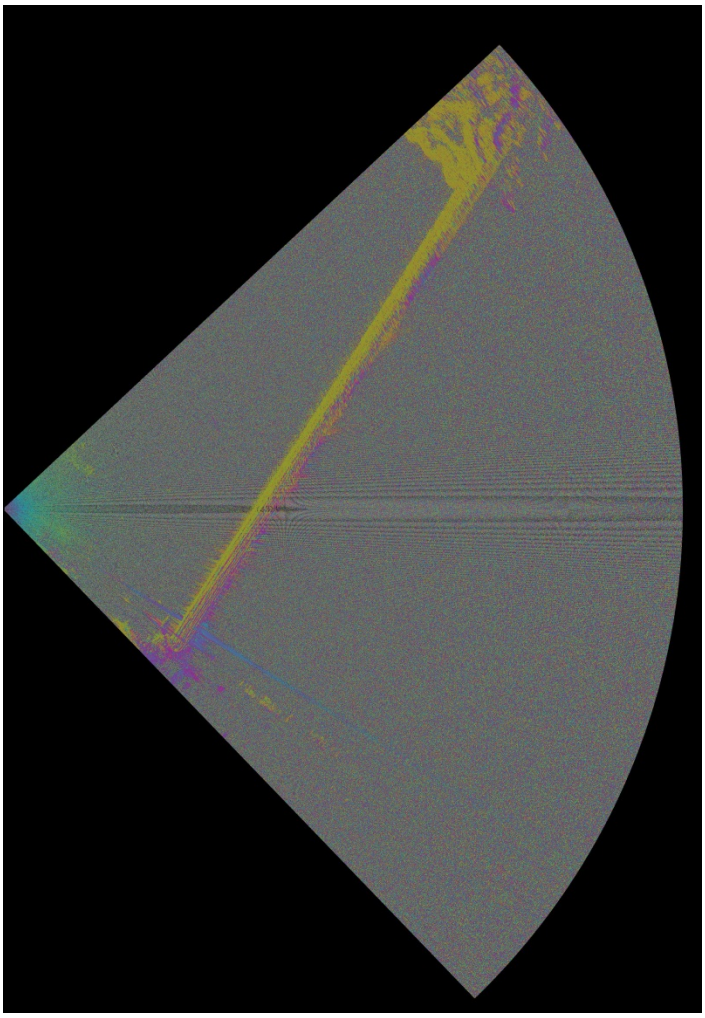

Figure 5-5.3. Ku-band single pass interferogram for Pin 1 at Milford Dam on 09/16/2011 is shown. The 2-m antenna is used.

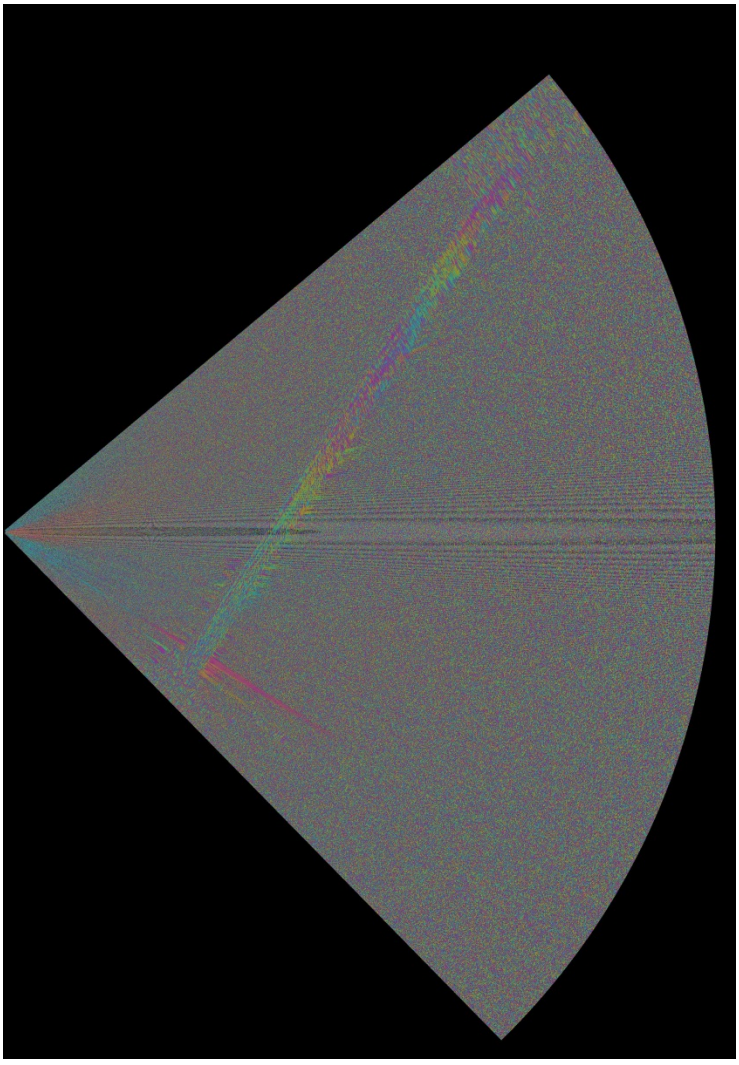

Figure 5-5.4. Ku-band repeat pass interferogram for Pin 1 at Milford Dam 09/16/2011-02/17/2012 is shown. The 2-m antenna is used.

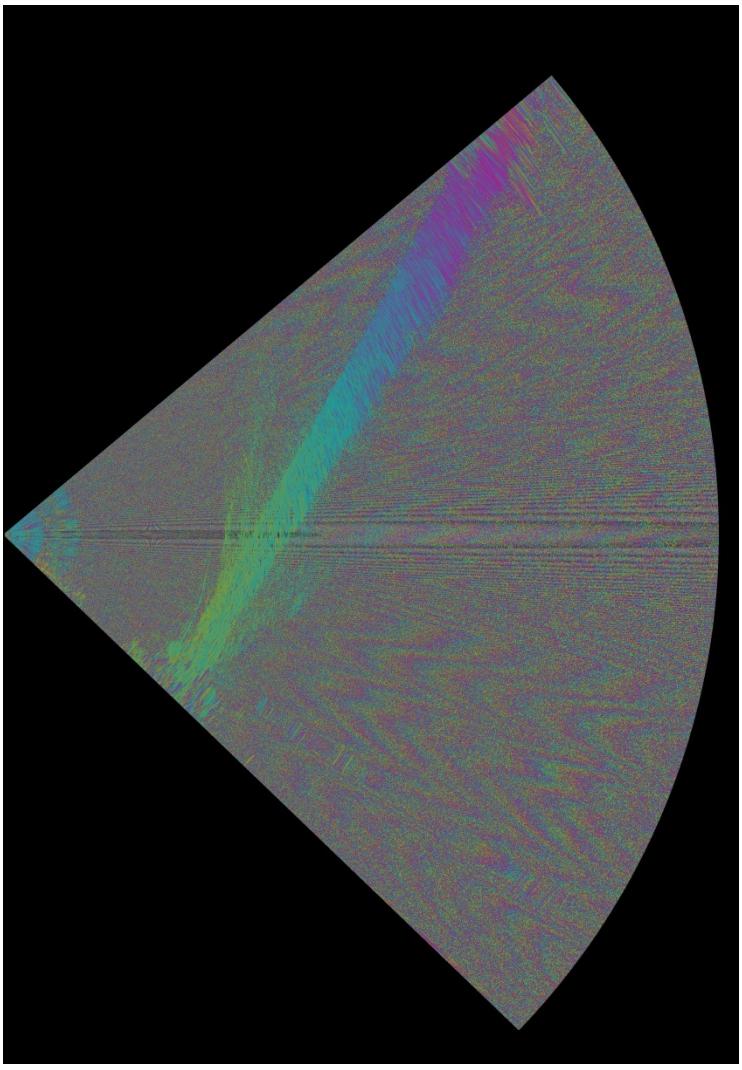

Figure 5-5.5. C-band (HH) repeat pass interferogram for Pin 1 at Milford Dam 11/18/2011-02/17/2012 is shown. The 2-m antenna is used.

5.5.2 Pin 3 at Milford Dam

At Pin 3, the GBIR scans the wall of the spillway at Milford Dam. Both Ku-band and C-band 2-m antennas were applied at this site. The maximum distance from the radar to the spillway is about 260 m. Figure 5-5.6 and Figure 5-5.7 are the Ku-band MLI images generated from the data collected at this site on 09/17/2011 in polar and rectangular coordinates, respectively. From Figure 5-5.7 the walls of the spillway

stretching out and the water area going through the spillway are distinguished.

Figure 5-5.8 is a single pass interferogram from the first scan on 09/17/2011. Coherence of the spillway is maintained in this image. Figure 5-5.9 shows a Ku-band repeat pass interferogram from two data sets collected from September, 2011 and February, 2012. The observed wall of the spillway in this interferogram is coherent during the repeat pass scans.

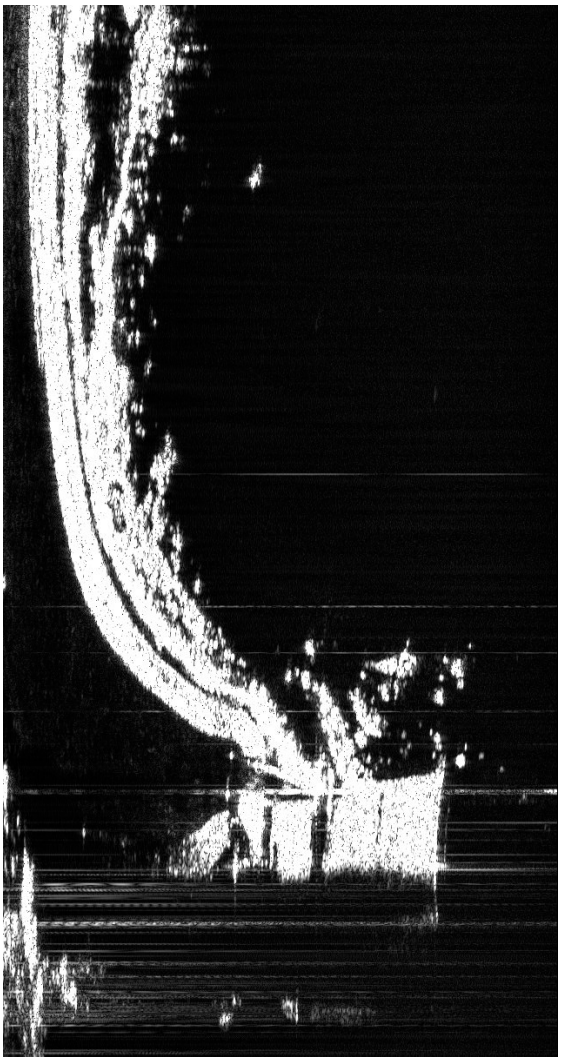

Figure 5-5.6. Ku-band MLI image in radar coordinates for Pin 3 at Milford Dam is shown. The 2-m antenna is used.

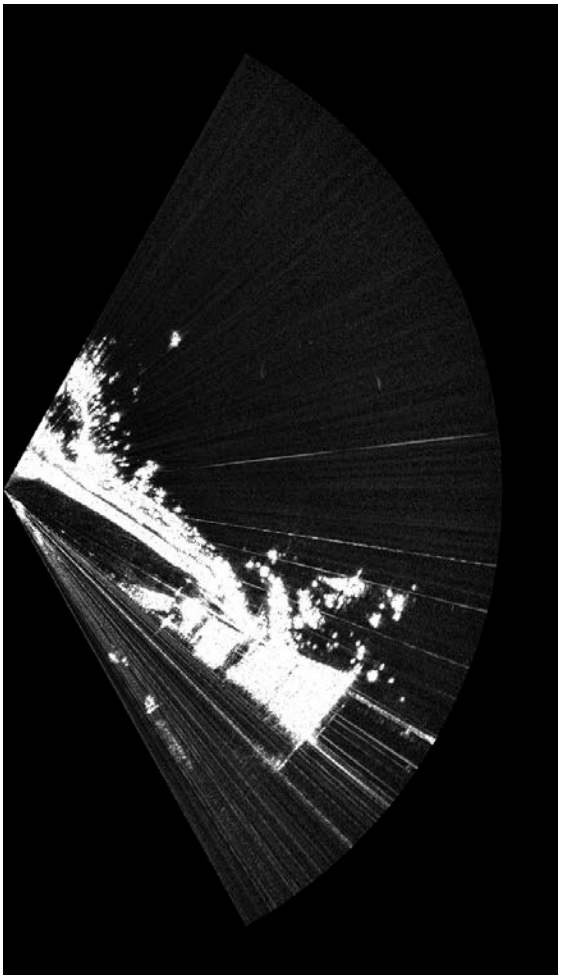

Figure 5-5.7. Ku-band MLI image in rectangular coordinates for Pin 3 at Milford Dam on 09/17/2011 is shown. The 2-m antenna is used.

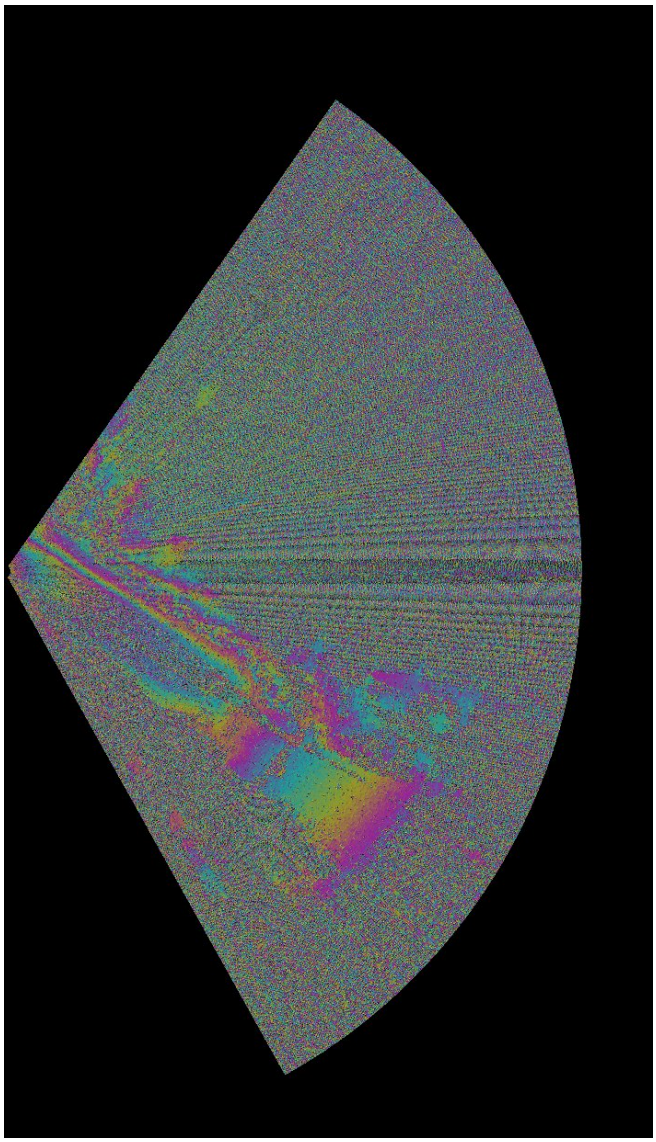

Figure 5-5.8. Ku-band single pass interferogram for Pin 3 at Milford Dam on 09/17/2011 is shown. The 2-m antenna is used.

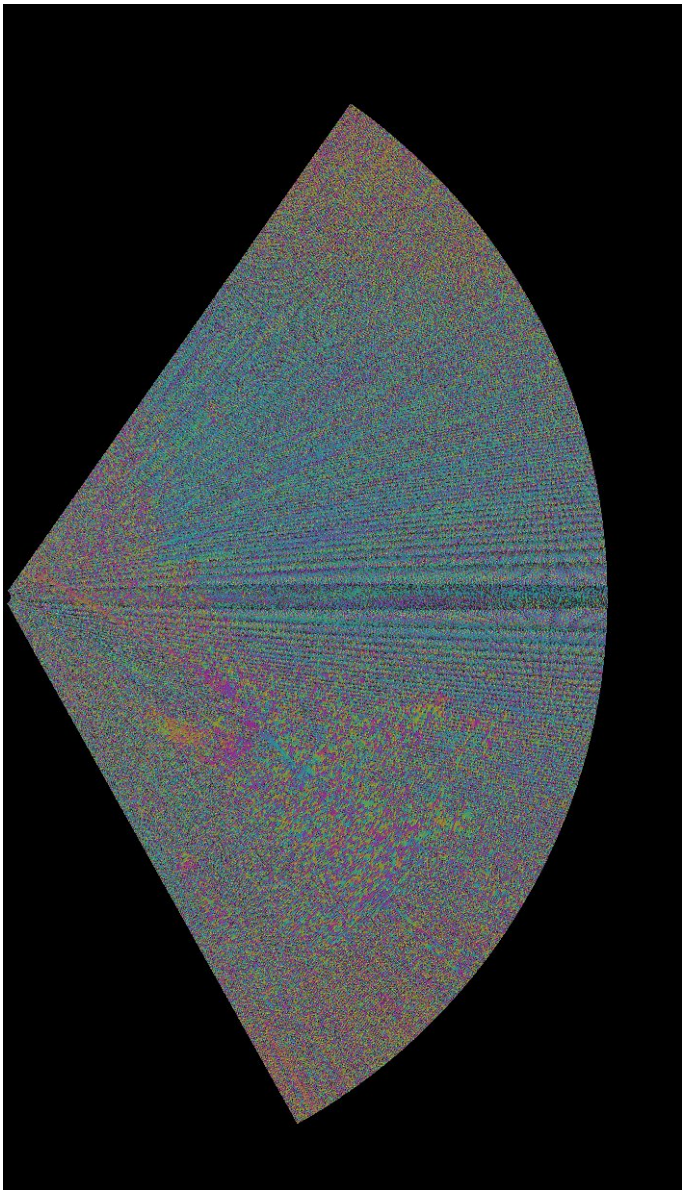

Figure 5-5.9. Ku-band repeat pass interferogram for Pin 3 at Milford Dam 09/17/2011-02/17/2012 is shown. The 2-m antenna is used.

5.5.3 Pin 5 at Milford Dam

At Milford dam Pin 5, the GBIR scans the riprap covered front face (upstream side) of the dam. Experimental setup is similar to that for Pin 1. Both Ku-band and C-band 2-m antennas were utilized at this site. The maximum distance from the radar to the

dam is about 1700 m. Figure 5-5.10 and Figure 5-5.11 are the Ku-band MLI images generated from the data collected at this site on 09/17/2011 in polar and rectangular coordinates. The whole dam as well as some vegetation at the farther end of the dam are observed in the imagery shown in Figure 5-5.11. C-band quad-polarized images are also available at this site. Figure 5-5.12 includes fully-polarized MLI images (from the top left to bottom right are HH, VH, HV, VV). By comparing these images, the co-polarized MLI images have slightly stronger intensity than the cross-polarized MLI images.

Figure 5-5.13 is a Ku-band single pass interferogram from one scan on 09/17/2011. Coherence of the dam is maintained during this scan. Figure 5-5.14 is a Ku-band repeat pass interferogram from the data sets from September, 2011 and February, 2012. It shows that the coherence of the dam is retained between the two different-time repeat scans. Figures 5-5.15 to Figure 5-5.18 are C-band fully polarized repeat pass interferograms from the data sets from October, 2011 and February, 2012. The image co-registrations for HH, VV, VH polarized SLCs went well and the corresponding interferograms look clear. The scene is also coherent in these interferograms. For the HV polarized case, however, the co-registration process performance was worse, and the interferogram coherence appears somewhat degraded. The side lobes of the antenna beam generate a few image artifacts in the scene.

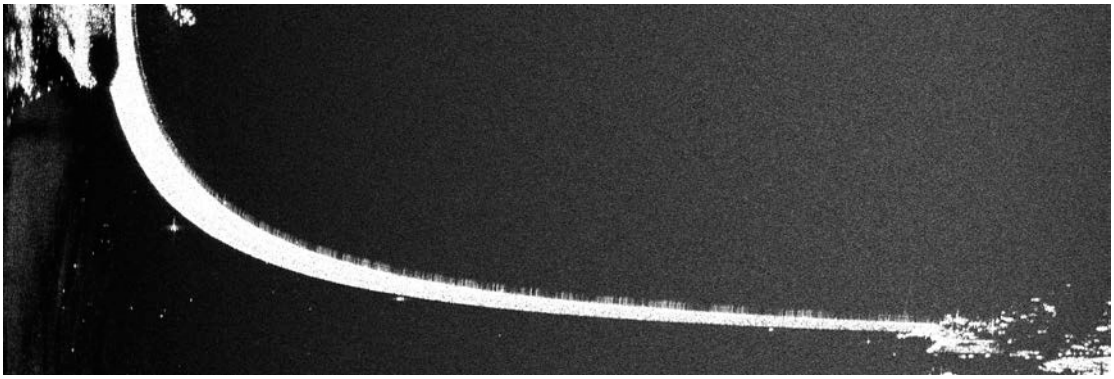

Figure 5-5.10. Ku-band MLI image in radar coordinates for Pin 5 at Milford Dam on 09/17/2011 is shown. The 2-m antenna is used.

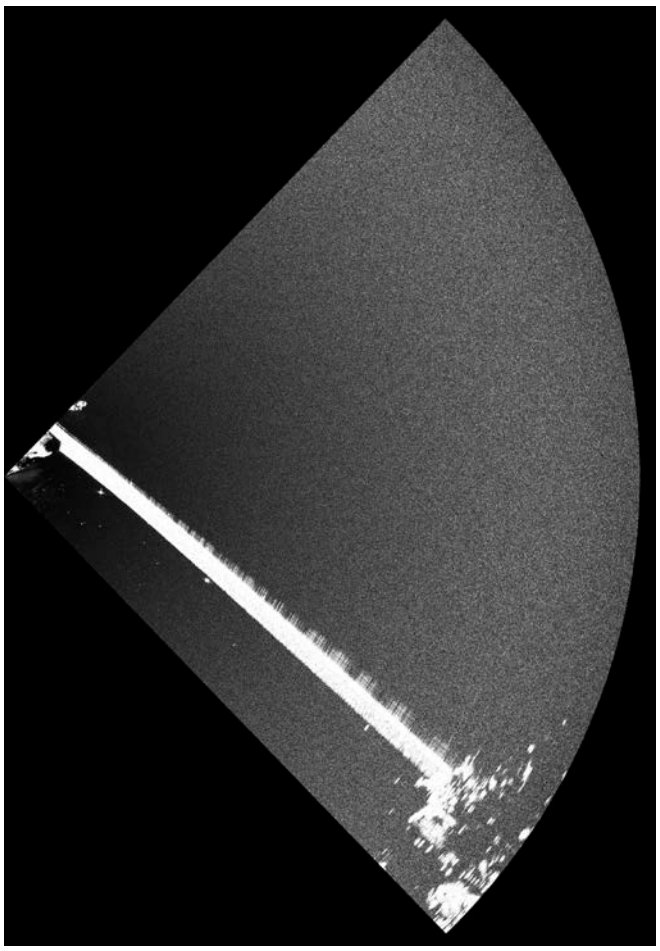

Figure 5-5.11. Ku-band MLI image in rectangular coordinates for Pin 5 at Milford Dam on 09/17/2011 is shown. The 2-m antenna is used.

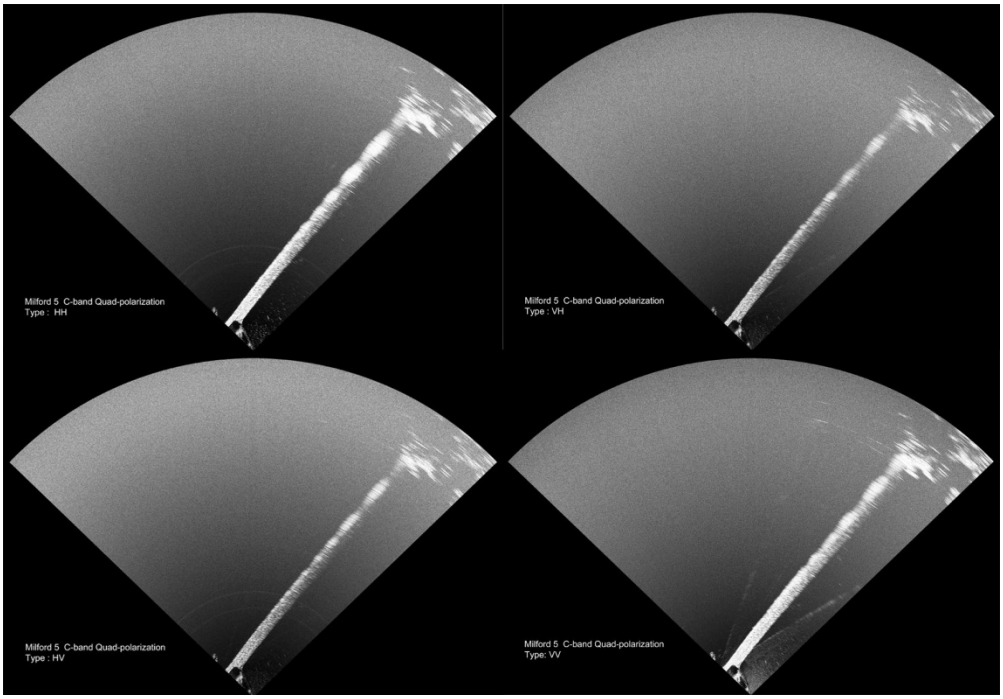

Figure 5-5.12. C-band fully polarimetric MLI images in rectangular coordinates for Pin 5 at Milford Dam on 10/07/2011(From left top to right bottom are HH, VH, HV, VV) are shown. The 2-m antenna is used.

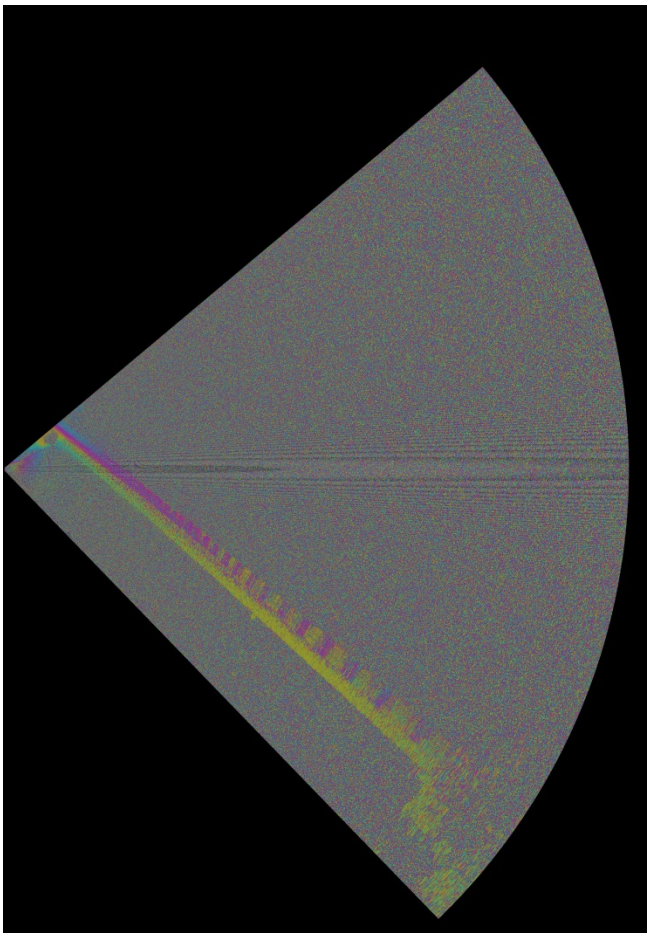

Figure 5-5.13. Ku-band single pass interferogram for Pin 5 at Milford Dam on 09/17/2011 is shown. The 2-m antenna is used.

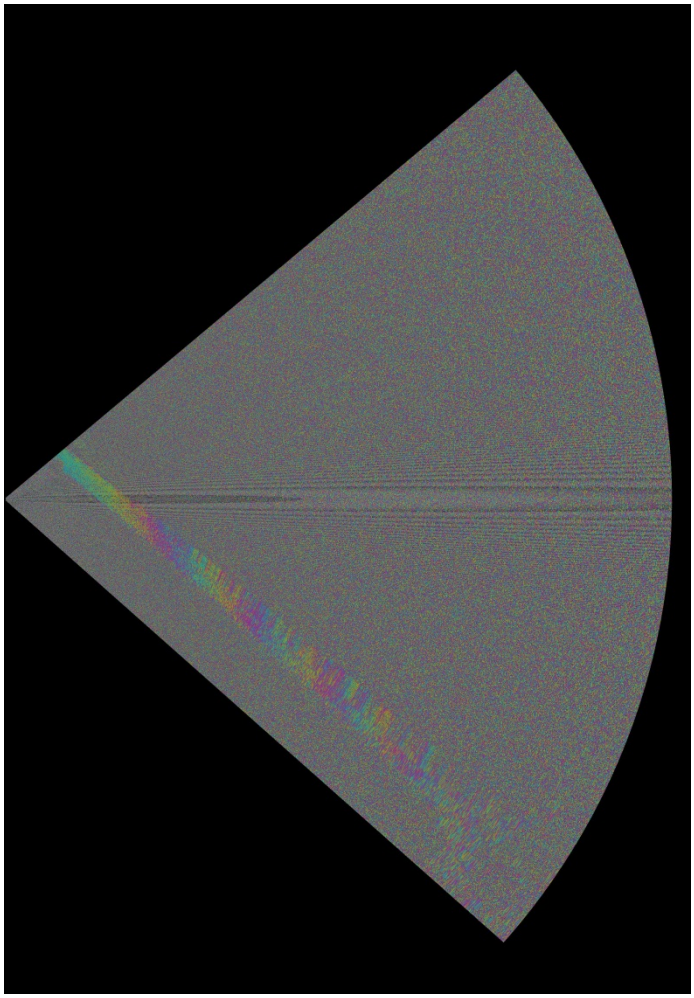

Figure 5-5.14. Ku-band repeat pass interferogram for Pin 5 at Milford Dam 09/17/2011-02/17/2012 is shown. The 2-m antenna is used.

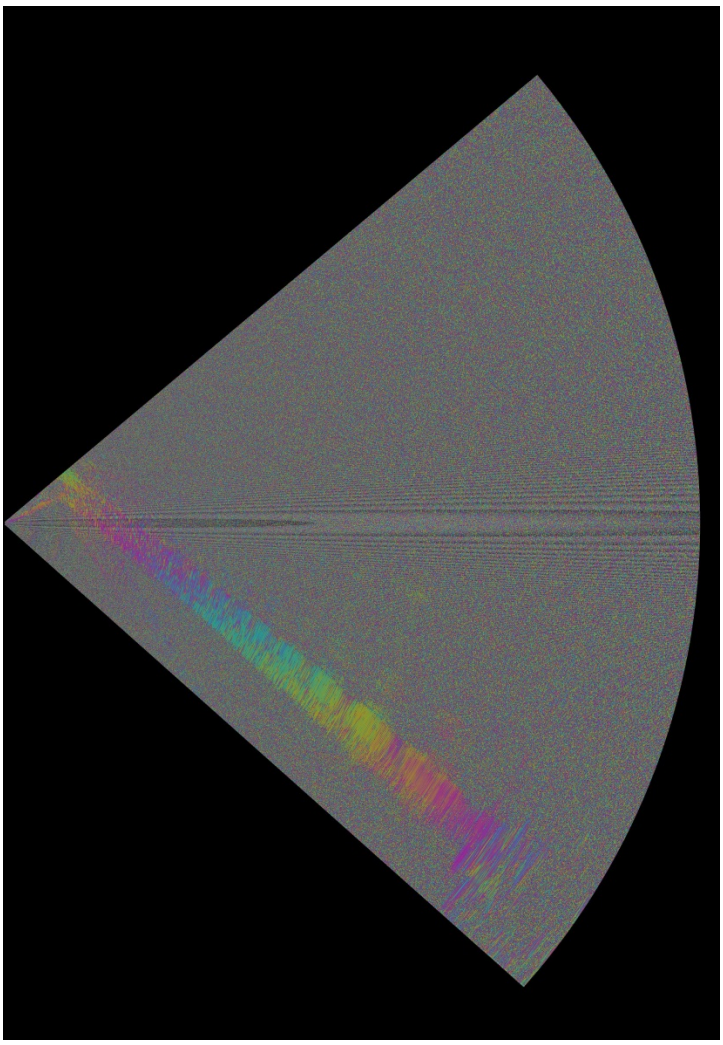

Figure 5-5.15. C-band(HH) repeat pass interferogram for Pin 5 at Milford Dam 10/07/2011-02/17/2012 is shown. The 2-m antenna is used.

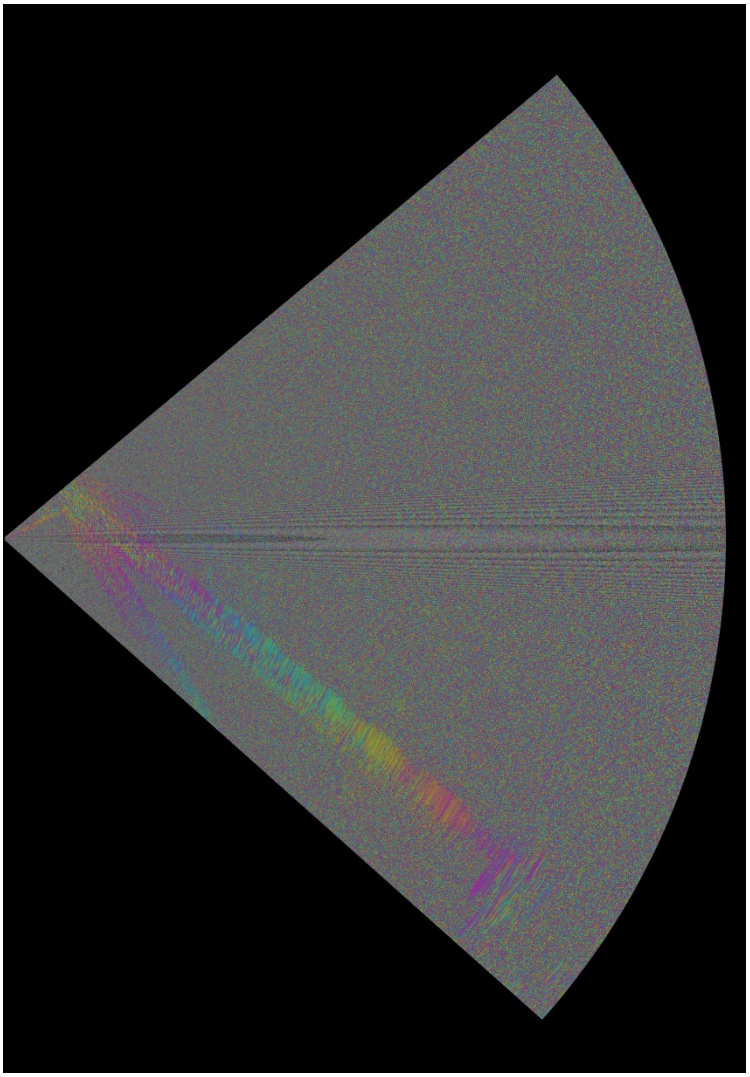

Figure 5-5.16. C-band(VH) repeat pass interferogram for Pin 5 at Milford Dam 10/07/2011-02/17/2012 is shown. The 2-m antenna is used.

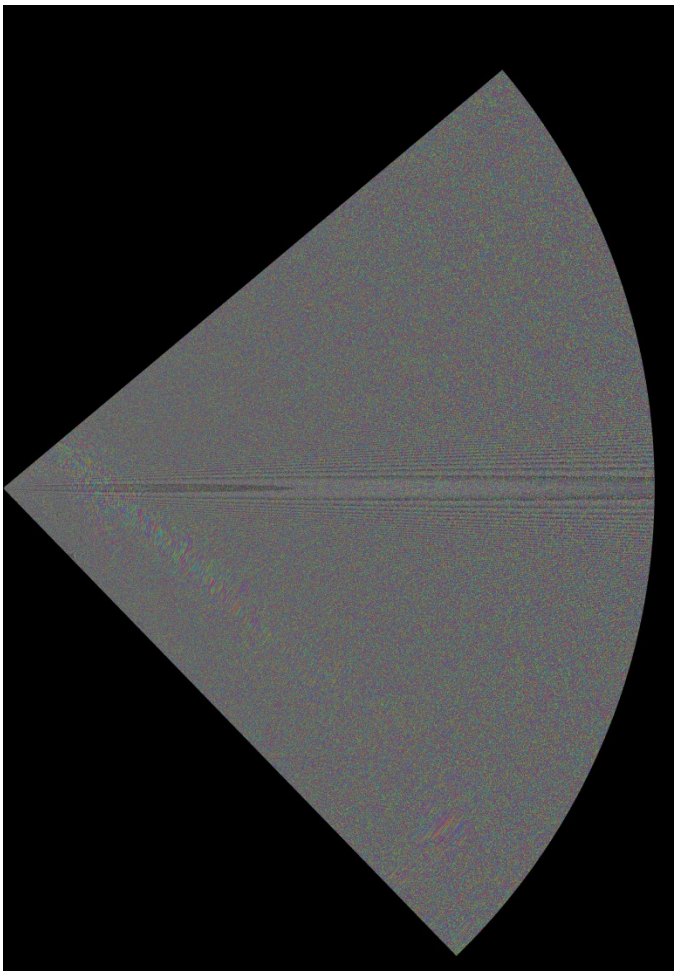

Figure 5-5.17. C-band(HV) repeat pass interferogram for Pin 5 at Milford Dam 10/07/2011-02/17/2012 is shown. The 2-m antenna is used.

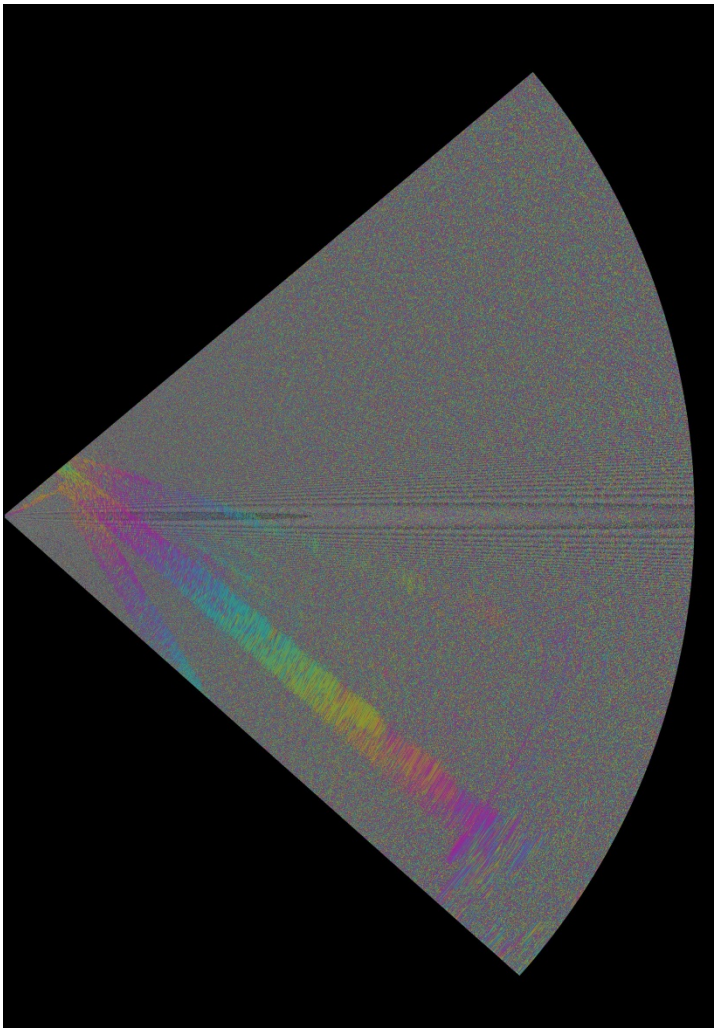

Figure 5-5.18. C-band (VV) repeat pass interferogram for Pin 5 at Milford Dam 10/07/2011-02/17/2012 is shown. The 2-m antenna is used.

5.6 Summary

Various GBIR image products were generated for each study site. The GBIR imaged the scene well at each site. Intensity images in polar and rectangular coordinates systems were generated for each site. Initial Ku-band and C-band interferometric products were generated for a number of sites. The interferograms show a strong coherence for most of the scenes imaged in this study. The initial

interferometric products will have topographical phase removed in later processing stages.

Chapter 6. Conclusion and Future Work

This thesis presented the initial image results from the Longview Dam, Blue Springs Dam, Tuttle Creek Dam, and Milford Dam experimental sites. The methods used for GBIR were presented. A number of system hardware and calibration target designs and motivation were presented. Excellent imaging performance of the MU GBIR has been observed for various target types such as riprap, concrete, soil, rock, metal, and vegetation. Furthermore, strong coherence of the test scene has been observed in the initial interferograms. Consequently, the initial GBIR products met expectation and design criteria.

Additional imagery may be gathered from the sites presented here and other sites. The portable nature of the GBIR system allows data collection in many locations. Future efforts may be enhanced by the initial lessons learned. As temporal time series with many images are collected, differential interferometry techniques may further enhance the GBIR products. Also, note that significant phase delay due to the atmosphere in the initial repeat pass interferograms has been discovered, which should be eliminated in future processing. After removing the phase delay caused by the atmosphere effects, the deformation of the scene could be readily obtained by studying the color cycles appearing in the interferogram. Furthermore, the initial

interferograms often show an amount of noise in the image, but could be reduced by applying filtering（e.g. adaptive spectral filtering）and phase unwrapping (e.g. phase unwrapping using Minimum Cost Flow and triangulation) methods in Gamma software. Furthermore, co-registration may be refined further for each pair of images. After generating, filtering and unwrapping all the interferograms for each pair of SLCs from two different time's data sets, advanced interferometry techniques can be utilized to linearly combine these interferograms together to generate an averaged interferogram, which may further reduce noise. Finally, a raster graphic image may be generated after combining the averaged interferogram together with the corresponding MLI image from the same scene to achieve better visual display effects.

In conjunction with the interferometric processing, future investigation exploring the dual-frequency measurements and polarimetric capabilities may yield interesting results. For instance, C-band interferograms with different polarization modes may be generated and compared for the study of polarimetric characteristics of different targets and scenes.

References

Cloude, S. and K. Papathanassiou (1998). “Polarimetric SAR Interferometry,” *IEEE Transactions on Geoscience and Remote Sensing*, vol. 36, no. 5, pp. 1551-1565.

Elachi, C., and Jakob van Zyl (2006). Introduction to the Physics and Techniques of Remote Sensing, John Wiley & Sons, Hoboken, New Jersey, 552 p.

GAMMA Remote Sensing AG (2011). GAMMA Portable Radar Interferometer II (GPIR-II), GAMMA Remote Sensing AG, Switzerland. Gamma website: http://www.gamma-rs.ch/

Hanssen, R. (2001). Radar Interferometry Data Interpretation and Analysis, Kluwer, Dordrecht, 201p, 308 p.

Fore, A., B. Chapman, S. Hensley, T. Michel, and R. Muellerschoeny (2009). “UAVSAR Polarimetric Calibration,” available: http://uavsar.jpl.nasa.gov/data/cal/UAV_cal.pdf

Mahafza, B. (2000). RADAR Systems Analysis and Design Using MATLAB, Chapman & Hall/CRC, 552 p.

Oppenheim, A. and R. Schafer (1989). Discrete-Time Signal Processing, Prentice Hall, Englewood Cliffs, New Jersey, 879 p.

Papathanassiou K., and M. Zink (1998). “Polarimetric Calibration of the Airborne Experimental SAR System of DLR,” *Proceedings of European SAR Conference*, EUSAR 1998, Friedrichshafen, Germany, pp. 259-262.

Richards, M. (2005). Fundamentals of RADAR Signal Processing, McGraw-Hill Companies, Inc., 513 p.

Skolnik, M. (1990). Radar Handbook. McGraw Hill, Boston, Massachusetts, 1200 p.

Quegan, S. (1994). “A Unified Algorithm for Phase and Cross-Talk Calibration of

Polarimetric Data-Theory and Observations," *IEEE Transactions on Geoscience and Remote Sensing*, Vol. 32, No.1, pp. 89-99.

van Zyl, J. and Y. Kim (2011). Synthetic Aperture Radar Polarimetry. John Wiley & Sons, Inc., Hoboken, New Jersey, 288 p.

Ulaby, F., R. K. Moore, and A. K. Fung (1982). Microwave Remote Sensing Active and Passive Volume II, Artech House, Norwood, MA, 1064 p.

Ulaby, F. (2007). Fundamentals of Applied Electromagnetics. Pearson Prentice Hall, Upper Saddle River, NJ, 464 p.

Appendix A GAMMA Software for GBIR Measurement and Data Processing

Various example GAMMA software codes and batch files are listed in this appendix.

A.1 Operating the GBIR Instrument through SSH for Data Collection

Table A.1. Operating the GBIR Instrument through SSH for Data Collection

(1) ssh –X gpri2 % log into the instrument through secure shell

(2) home_run.py % initiate home run of the positioner, the instrument is looking
% at 0 degrees instrument azimuth angle after home-run

(3) cd /data % get access into data directory
mkdir <location name> % create a new directory for data collection and
% processing
cd <location name> % move into the directory

(4) cp ../data/profiles/gpri_500us.prf . % copy profile template to current directory，
%take gpri_500us.prf as an example

(5) chmod +rwx gpri_500us.prf % enable editing the copied profile
gedit gpri_500us.prf % edit the profile

(6) gpri2_capture_all.pl gpri_500us.prf RAW_1 1 1 15 % run a first scan

(7) gpri2_plot.py –s 100 gpri_500us.prf 20110927_1.raw % check signal
% levels in gpri2_plot o make sure there is no saturation and that there is
% sufficient signal and adjust attenuation setting in the prf file. Redo step (5)/(6)
% until gain is ok.

(8) gpri2_capture_all.pl gpri_500us.prf RAW_1 2 10 15 % if the
%attenuation is OK, go for repeat measurements

(9) home_run.py % always do a positioner home-run before shutting down the
%instrument

(10) sudo shutdown –P now % shut down the Instrument Controller

A.2 GAMMA Commands for Ku-band Data Processing (Ku-band Raw Data from Milford Pin5, 20120217)

Table A.2. GAMMA Commands for Ku-band Data Processing (Ku-band Raw Data from Milford Pin5, 20120217)

```
$ mkdir practice_Ku    % make a new directory named practice_Ku for data
                       % processing
$ cd practice_Ku           % go to the new directory
$ ln -s ../gpri_1ms.prf .      % make a symbolic link for the profile
$ ln -s ../RAW_Ku5 .          % make a symbolic link for the raw files
$ ls -1 RAW_Ku5/*.raw > q1
$ ls -1 RAW_Ku5/*.raw_par > q2
$ paste q1 q2 > RAW_list    % create the RAW_list

$ gpri2_proc_all.pl RAW_list SLC_20120217 - 10 225 SLC_tab proc.log
  % image processing for the raw data, use a decimation factor of 10 to get the SLCs
$ mk_mli_all SLC_tab MLI_20120217 1 1    % generate MLI images from the set of
                                         % SLCs generated from the former step
$ cd MLI_20120217
$ gedit 20120217_001l.mli.par      % check the MLI parameter file to get the value for
                                   % range_pixel_spacing
$ pol2rec 20120217_001l.mli 20120217_001l.mli.par 20120217_001l.rec 20120217_001l.rec.par 0.75 0    % convert the intensity image from polar coordinates
                                   %to rectangular coordinates. The value used for
                                   %pixel size is equal to range_pixel_spacing in MLI
                                   %parameter file
$ gedit 20120217_001l.rec.par      % check the parameter file for the value of
                                   % range_samples
$ raspwr 20120217_001l.rec 2813    % generate the raster graphics image of intensity
                                   % data, the width of the image is equal to the
                                   % value of range_samples acquired from last
                                   %step
$ gimp 20120217_001l.rec.ras         % display the raster file using GNU Image
                                   % Manipulation Program
```

A.3 GAMMA Commands for C-band Data Processing(C-band Quad Polarimetric Data from Milford Pin 5, 20120217)

Table A.3. GAMMA Commands for C-band Data Processing(C-band Quad Polarimetric Data from Milford Pin 5, 20120217)

```
$ mkdir SLC_20120217_cquad          % make a new directory for the SLCs
$ cd    SLC_20120217_cquad
$ gpri2_proc.py ../rawChv/20120217_001.raw ../rawChv/20120217_001.raw_par 20120217_001Vl.slc 20120217_001Vu.slc -d 5
-t V
% process raw data to SLCs, use a decimation factor of 5 and TX_ANTENNA mode
% is set to V: transmitting vertically polarized pulses
$ gpri2_proc.py ../rawChv/20120217_001.raw ../rawChv/20120217_001.raw_par 20120217_001Hl.slc 20120217_001Hu.slc -d 5
-t H
% process raw data to SLCs, use a decimation factor of 5 and TX_ANTENNA mode
% is set to H: transmitting horizontally polarized pulses
$ mk_tab SLC_20120217_cquad slc slc.par SLC_tab    % generate SLC tab for
                                                    %processing
$ mk_mli_all SLC_tab MLI_20120217_cquad 1 1    % generate MLI images from a
                                                % set of SLCs
$ cd MLI_20120217_cquad/
$ gedit 20120217_001Hl.mli.par       % check the MLI parameter file for the value of
                                     % range_pixel_spacing
$ pol2rec 20120217_001Hl.mli 20120217_001Hl.mli.par 20120217_001Hl.rec 20120217_001Hl.rec.par 0.75 0       % convert
the coordinates from polar to
                                   % rectangular for the MLI image
$ gedit 20120217_001Hl.rec.par     % check the parameter file for the value of
                                   % range_samples
$ raspwr 20120217_001Hl.rec 2813      % Generate the raster graphics image for the
                                      % MLI image
$ gimp 20120217_001Hl.rec.ras         % display the raster image in the GNU Image
                                      % Manipulation Program
```

A.4 GAMMA Commands for Image Co-registration and Interferogram Generation

Table A.4. GAMMA Commands for Image Co-registration and Interferogram Generation

$ create_offset 20110917_003l.slc.par 20120217_001l.slc.par 20110917_003l-20120217_001l.off
% offset parameter file creation, when running this command, keep hitting 'Enter'
% button, other associated parameters were set to default values.

$ dis2SLC 20110917_003l.slc 20120217_001l.slc 2747 2747 - - - - - - 0
% alternating display of two SLC images, use "gedit" to check the SLC parameter file
% for the widths of the two SLCs. Use default for all the other options in this
% command first. After running this command, find the initial offset by alternately
% switching from one image to other. A tip for getting a more precise offset is to
% choose a specific point in one image, record its coordinates and then switch to the
% other image to find the coordinates of the same point. The difference of these
% coordinates for the same point are the initial offsets.
$ dis2SLC 20110917_003l.slc 20120217_001l.slc 2747 2747 - - 0 44 - - 0
% rerun this command, use the calculated offsets for the roff and azoff parameters (in
% this case, they are 0 and 44, respectively). Alternately switching these two images,
% observe the offset by eye. Change the offset values again and keep running the
% command until the visual offsets can be controlled within a few pixels. Also,
% choose a point within the interested area as the center of the patch. Record the
% coordinates of the point for next step.

$ init_offset 20110917_003l.slc 20120217_001l.slc 20110917_003l.slc.par 20120217_001l.slc.par 20110917_003l-20120217_001l.off 1 1 459 480 0 44 –
% Determine initial offset between two SLC images using correlation of image
% intensity. The center of the patch was set to 459 in range, 480 in azimuth and the
% initial offsets in range and azimuth were set to 459 and 480, respectively. Other
% parameters were set to their default values.

$ offset_pwr 20110917_003l.slc 20120217_001l.slc 20110917_003l.slc.par 20120217_001l.slc.par 20110917_003l-20120217_001l.off 20110917_003l-20120217_001l.offs 20110917_003l-20120217_001l.snr 20 20 - 2 40 80 6.0 0| tee 20110917_003l-20120217_001l.txt
% Estimate the range and azimuth registration offset using intensity cross-correlation.
% Search window size was set to 20 pixels by 20 pixels. Total number of offset
% estimates was set to 40×80. The offset estimation threshold used was 6.0. The
%processing history was saved in a text file named

% 20110917_003l-20120217_001l.txt.

$ offset_fit 20110917_003l-20120217_001l.offs 20110917_003l-20120217_001l.snr 20110917_003l-20120217_001l.off 20110917_003l-20120217_001l.coffs 20110917_003l-20120217_001l.coffsets 6.0 3 0
% compute range and azimuth registration offset polynomials. In this case, it derived
% the 3-parameter regression polynomials with a minimum SNR threshold of 6.0
% without using the interactive culling.

$ offset_fit 20110917_003l-20120217_001l.offs 20110917_003l-20120217_001l.snr 20110917_003l-20120217_001l.off 20110917_003l-20120217_001l.coffs 20110917_003l-20120217_001l.coffsets 6.0 3 1
% rerun the same command using interactive culling this time by manually setting the
% range error threshold and azimuth error threshold until the model fit standard
% deviation is less than 0.1 for both range and azimuth.

$ SLC_interp 20120217_001l.slc 20110917_003l.slc.par 20120217_001l.slc.par 20110917_003l-20120217_001l.off 20120217_001l.rslc 20120217_001l.rslc.par | tee -a 20110917_003l-20120217_001l.txt
% resample the SLCs using 2-D SINC interpolation and register SLC-2 to the
% reference geometry. Also, save the processing history into
% 20110917_003l-20120217_001l.txt

$ create_offset 20110917_003l.slc.par 20120217_001l.rslc.par 20110917_003l_r-20120217_001l_r.off
% create the new offset parameter file for the resampled slcs

$ mkdir INT-test % make a new directory to store the interferogram

$ interf_SLC ../RSLC-l/20110917_003l.slc ../RSLC-l/20120217_001l.rslc ../RSLC-l/20110917_003l.slc.par ../RSLC-l/20120217_001l.rslc.par ../RSLC-l/20110917_003l_r-20120217_001l_r.off 20110917_003l.pwr 20120217_001l.pwr 20110917_003l-20120217_001l.int 1 1 > test1.out
% Co-register 20120217_001l.rslc to 20110917_003l.slc again and compute the
% multi-look complex interferogram and co-registered power images.

& gedit test1.out % check the .out file for the number of lines in the interferogram
$ cp ../../../../../kansas-09-16/milford_5/practice_Ku/MLI/20110917_003l.mli.par .
$ gedit 20110917_003l.mli.par &
% copy and edit the corresponding parameter file and save it as a new interferogram
% parameter file named 20110917_003l-20120217_001l.int.par

$ pol2rec 20110917_003l-20120217_001l.int 20110917_003l-20120217_001l.int.par 20110917_003l-20120217_001l.int.rec 20110917_003l-20120217_001l.int.rec.par 0.75 1
% convert the interferogram from polar coordinates to rectangular coordinates
$ gedit 20110917_003l-20120217_001l.int.rec.par
% check the parameter file for the value of range_samples
$ rasmph 20110917_003l-20120217_001l.int.rec 2813

```
% Generate a raster graphics image of the phase and intensity of complex data
$ gimp 20110917_003l-20120217_001l.int.rec.ras
% display the raster interferogram image in the GNU Image Manipulation Program
```

Appendix B The List of Values for Parameters Associated with the Decimation Factor for Each Test Site

Table Appendix B-1. Decimation information is shown.

Site	$\Delta\theta$(degrees/line)	β_{az}(degrees)	K	D
Longview Pin1	5.041943e-03	0.5	0.7900	20
Longview Pin3	2.524197e-03	10	0.9897	40
Longview Pin4	2.524197e-03	10	0.9897	40
Longview Pin5	2.524197e-03	0.5	0.7980	40
Blue Springs Pin2(C quad)	5.074693e-03	1.5	0.8000	59
Tuttle Creek Pin1	1.008227e-02	0.5	0.7900	10
Tuttle Creek Pin5	5.041943e-03	0.5	0.7900	20
Milford Pin1	1.008227e-02	0.5	0.7900	10
Milford Pin1(C hh)	1.008227e-02	1.5	0.9300	10
Milford Pin3	2.524197e-03	0.5	0.7980	40
Milford Pin5	1.008227e-02	0.5	0.7900	10
Milford Pin5(C quad)	2.016455e-02	1.5	0.9300	5